STRUCTURAL BIOLOGY

De novo macrocyclic peptides for inhibiting, stabilizing, and probing the function of the retromer endosomal trafficking complex

Kai-En Chen[1], Qian Guo[1]†, Timothy A. Hill[1,2]†, Yi Cui[3], Amy K. Kendall[4,5], Zhe Yang[3], Ryan J. Hall[1], Michael D. Healy[1], Joanna Sacharz[6], Suzanne J. Norwood[1], Sachini Fonseka[1], Boyang Xie[4,5], Robert C. Reid[1,2], Natalya Leneva[1]‡, Robert G. Parton[1,7], Rajesh Ghai[1]§, David A. Stroud[6,8], David P. Fairlie[1,2], Hiroaki Suga[9], Lauren P. Jackson[4,5], Rohan D. Teasdale[3], Toby Passioura[9,10], Brett M. Collins[1]*

The retromer complex (Vps35-Vps26-Vps29) is essential for endosomal membrane trafficking and signaling. Mutation of the retromer subunit Vps35 causes late-onset Parkinson's disease, while viral and bacterial pathogens can hijack the complex during cellular infection. To modulate and probe its function, we have created a novel series of macrocyclic peptides that bind retromer with high affinity and specificity. Crystal structures show that most of the cyclic peptides bind to Vps29 via a Pro-Leu–containing sequence, structurally mimicking known interactors such as TBC1D5 and blocking their interaction with retromer in vitro and in cells. By contrast, macrocyclic peptide RT-L4 binds retromer at the Vps35-Vps26 interface and is a more effective molecular chaperone than reported small molecules, suggesting a new therapeutic avenue for targeting retromer. Last, tagged peptides can be used to probe the cellular localization of retromer and its functional interactions in cells, providing novel tools for studying retromer function.

INTRODUCTION

Endosomal compartments serve as central hubs for transmembrane protein and lipid sorting and as platforms for cell signaling. Transmembrane protein cargos that arrive in the endosomal network via endocytosis or anterograde trafficking are routed either for lysosomal degradation or recycling to other compartments including the trans-Golgi network and the cell surface. Endosomal trafficking thus plays a pivotal role in maintaining cellular homeostasis, and this is controlled by a number of essential protein machineries (*1*–*3*).

The evolutionarily conserved retromer complex composed of Vps26, Vps29, and Vps35 is a master regulator of endosomal dynamics responsible for cargo sorting and recycling within tubulovesicular transport carriers (*2*, *4*–*8*) and, in higher eukaryotes, cooperates with an array of cargo adaptors and accessory proteins to allow membrane recruitment, cargo sorting, and trafficking to occur (*2*, *3*, *9*). The known cargo adaptors are derived from the sorting nexin (SNX) protein family and include SNX3 and SNX27.

Retromer mutation or dysregulation in humans leads to defective endosomal and lysosomal function implicated in neurodegenerative disorders including Parkinson's disease (PD) (*10*–*15*), Alzheimer's disease (AD) (*16*–*19*), and amyotrophic lateral sclerosis (ALS) (*20*). Retromer dysfunction affects endosomal and lysosomal homeostasis in neurons and microglia in multiple ways (*11*, *21*), involving deficits in regulatory protein interactions such as WASH and leucine-rich repeat kinase 2 (*14*, *22*, *23*), missorting of specific endosomal cargos (*10*, *24*–*27*), defects in mitochondrial function and mitophagy (*28*–*31*), and other widespread deficiencies in lysosomal and autophagic degradation of toxic material (*14*, *17*, *19*, *32*–*34*). Retromer is also a prominent target hijacked by intracellular pathogens to facilitate their transport and replication. This includes viruses such as SARS-CoV-2 (severe acute respiratory syndrome coronavirus 2), HIV, HCV (hepatitis C virus), and HPV (human papillomavirus) (*35*–*39*) and intracellular bacteria such as *Coxiella burnetii* and *Legionella pneumophila* (*40*–*44*). Mechanistic studies have shown that the secreted effector protein RidL from *L. pneumophila* binds directly to Vps29, competing with endogenous regulators TBC1D5 and VARP, inhibiting retromer-mediated cargo transport, and supporting the growth of *L. pneumophila* in intracellular endosome-derived vacuoles (*40*, *41*, *43*, *44*). Similarly, the minor capsid protein L2 from HPV is thought to hijack retromer-SNX3–mediated endosomal transport by mimicking sequence motifs found in endogenous cargos such as the cation-independent mannose 6-phosphate receptor (CI-MPR) and divalent metal transporter 1-II (DMT1-II) (*38*, *45*).

Given the importance of retromer in endosomal trafficking, neurodegenerative disease, and cellular infection, there is substantial interest in developing molecular approaches to either inhibit or enhance retromer activity. Inhibition of retromer may provide a novel avenue for targeting infectious pathogens. For example, peptide-based inhibitors of retromer, derived from the HPV L2

[1]Institute for Molecular Bioscience, The University of Queensland, St. Lucia, Queensland 4072, Australia. [2]ARC Centre of Excellence for Innovations in Peptide and Protein Science, Institute for Molecular Bioscience, The University of Queensland, St. Lucia, Queensland 4072, Australia. [3]School of Biomedical Sciences, The University of Queensland, St Lucia, Queensland 4072, Australia. [4]Department of Biological Sciences, Vanderbilt University, Nashville, TN 37232, USA. [5]Center for Structural Biology, Vanderbilt University, Nashville, TN 37232, USA. [6]Department of Biochemistry and Molecular Biology, Bio21 Molecular Science and Biotechnology Institute, University of Melbourne, Parkville, Victoria 3052, Australia. [7]Centre for Microscopy and Microanalysis, The University of Queensland, Queensland, Australia. [8]Murdoch Children's Research Institute, The Royal Children's Hospital, Parkville, Victoria 3052, Australia. [9]Department of Chemistry, Graduate School of Science, The University of Tokyo, 7-3-1 Hongo, Bunkyo-Ku, Tokyo 113-0033, Japan. [10]Sydney Analytical, School of Life and Environmental Sciences and School of Chemistry, The University of Sydney, Camperdown, New South Wales 2050, Australia.
*Corresponding author. Email: b.collins@imb.uq.edu.au
†These authors contributed equally to this work.
‡Present address: Cambridge Institute for Medical Research, Cambridge CB2 0XY, UK.
§Present address: CSL Ltd, Parkville, Victoria 3052, Australia.

protein, are able to reduce infection by slowing the normal retrograde transport of incoming virions (*38*, *45*). Conversely, because of its neuroprotective role, retromer-binding "molecular chaperones" may be used to enhance retromer function in diseases including AD, PD, and ALS, with the goal of boosting normal endosome-dependent clearance pathways to reduce accumulation of toxic aggregates of proteins such as β amyloid (Aβ), tau, and α-synuclein (*46*, *47*). Previously, a small molecule called R55 (also called TPT-260) was identified, which can bind with modest affinity to retromer at the interface between Vps35 and Vps29 and stabilize its structure (*48*). This molecule has since been shown to have activity in stabilizing retromer in cells and, as predicted, can enhance the transport of essential receptors and reduce the accumulation of toxic material including Aβ and α-synuclein in cell, fly, and mouse models (*33*, *48*–*51*). Recently, a derivative of R55 was found to improve retromer stability and lysosomal dysfunction in a model of ALS (*20*). Nonetheless, the low potency and specificity of these compounds mean that other molecules are actively being sought.

We have adopted a screening strategy, referred to as the RaPID (random nonstandard peptides integrated discovery) system, to identify a series of eight de novo macrocyclic peptides with high affinity and specificity for retromer, having either inhibitory or stabilizing activities. These peptides bind to retromer with affinities [dissociation constant (K_d)] ranging from 0.2 to 850 nM and can be classified into two groups on the basis of their binding sites. Most interact specifically with the Vps29 subunit, and crystal structures show that these peptides associate with a highly conserved pocket on Vps29 that is also used by the accessory proteins TBC1D5 and VARP, as well as the bacterial protein RidL, and are potent inhibitors of their binding. We also identified one peptide, RT-L4, that shows in vitro activity as a molecular chaperone. RT-L4 stabilizes retromer assembly via binding to the interface between Vps26 and Vps35, does not disrupt retromer's association with known accessory proteins and cargo adaptors, and indeed allosterically enhances binding to several ligands including SNX27 and TBC1D5. Last, using reversible cell permeabilization and fluorescent peptides, we demonstrate that they specifically colabel Vps35-positive endosomal structures, can perturb endosomal recruitment of TBC1D5 by retromer, and can be used as baits for isolating retromer from cells. These macrocyclic peptides thus provide novel research tools and suggest potential new avenues for developing therapeutic modifiers of retromer function.

RESULTS

Identification of highly potent retromer-binding macrocyclic peptides

The procedure of the RaPID system (Fig. 1A) exploits the diverse molecular topology of macrocyclic peptide populations numbering $>10^{12}$ unique sequences to enrich for and amplify low-abundance, high-affinity ligands (*23*, *52*–*55*). We performed the RaPID selection using purified His-tagged human retromer complex as bait: A puromycin-linked semirandomized mRNA library, of the general form AUG-$(NNK)_{4-15}$-UGC, was translated in an in vitro translation reaction to generate peptides covalently linked to their cognate mRNAs through the puromycin moiety. Macrocyclization was effected through genetic code reprogramming of initiating AUG (methionine) codons to incorporate either *N*-chloroacetyl-L-tyrosine (ClAc-L-Tyr) or *N*-chloroacetyl-D-tyrosine (ClAc-D-Tyr), leading to a spontaneous reaction with a downstream UGC-encoded cysteine to form a library of thioether-bridged cyclic peptides each linked to their cognate mRNA (total diversity of $>10^{12}$ molecules). Retromer ligands were then identified through iterative cycles of affinity selection against immobilized retromer complex followed by reverse transcription polymerase chain reaction (PCR) recovery, transcription, and regeneration of peptide-mRNA fusion libraries, with deconvolution of the final enriched library achieved through next-generation sequencing.

We selected the four most abundant peptides from each of the ClAc-L-Tyr– or ClAc-D-Tyr–initiated libraries (Fig. 1B, fig. S1, and table S1) for further characterization, and each was synthesized using standard 9-fluorenyl methoxycarbonyl (Fmoc) chemistry. These were validated against the retromer complex by surface plasmon resonance (SPR), and all were confirmed to bind very strongly to retromer with affinities (K_ds) in the range of <0.2 to 30 nM (fig. S2). Secondary SPR comparisons showed that these molecules also bound the purified retromer complex from *Danio rerio* (zRetromer) (fig. S2) and the thermophilic yeast *Chaetomium thermophilum* (ctRetromer) with a similar range of binding affinities, indicating that they associate with evolutionarily conserved sites in the complex.

Macrocyclic peptide binding to retromer was validated using isothermal titration calorimetry (ITC). Among the eight cyclic peptides tested, six were confirmed to bind retromer with nanomolar binding affinity, while the peptides RT-D4 and RT-L3 were not sufficiently soluble for ITC experiments (Fig. 1, C and D, and table S2). Affinities for retromer measured by ITC were systematically lower but correlated well with those measured by SPR, ranging from 25 to 850 nM. These affinities are comparable to or better than the high affinities for the retromer binding regulatory protein TBC1D5 (220 nM) (*56*) or the bacterial effector RidL (150 nM) (*43*, *44*).

The retromer structure consists of a long Vps35 α-helical solenoid, with Vps26A or Vps26B bound to the N terminus and Vps29 bound at the C terminus (Fig. 1E) (*57*–*61*). We examined the specific subunits of retromer required for binding each of the cyclic peptides by testing either Vps29 alone, Vps26A alone, the Vps35-Vps29 heterodimer, or subcomplexes of Vps26A with N-terminal fragments of Vps35 (Fig. 1D and table S1). Full-length Vps35 is relatively unstable on its own and was not tested separately. RT-D1, RT-D2, RT-D3, RT-L1, and RT-L2 all bind specifically to either Vps29 alone or to the Vps35-Vps29 heterodimer, but not to Vps26A. Their affinities for Vps29 alone were not significantly different to their binding to the retromer holo-complex or Vps35-Vps29 heterodimer, ranging from 8 to 783 nM. This indicates that they bind specifically and exclusively to the Vps29 subunit. Although peptides RT-D4 and RT-L3 were not tested for binding specific subunits, it is likely they also bind to Vps29 as they have a Pro-Leu motif that we show below that mediates Vps29 interaction by the other five peptides (Fig. 1, B and E).

In contrast to other peptides, RT-L4 did not bind to any of the retromer subunits individually or to the Vps35-Vps29 dimer, but rather only to subcomplexes that contained both Vps26A and Vps35 (Fig. 1C). N-terminal fragments of Vps35 in complex with Vps26A, including $Vps35_{1-390}$ and $Vps35_{1-224}$, supported binding to the RT-L4 peptide with a similar affinity to the retromer trimeric holo-complex, while $Vps35_{1-390}$ on its own did not (Fig. 1D). When Vps35 was truncated to the shortest region still capable of Vps26A interaction ($Vps35_{1-172}$), a small but consistent decrease in binding affinity was observed, suggesting that α helix 8 in Vps35 (residues

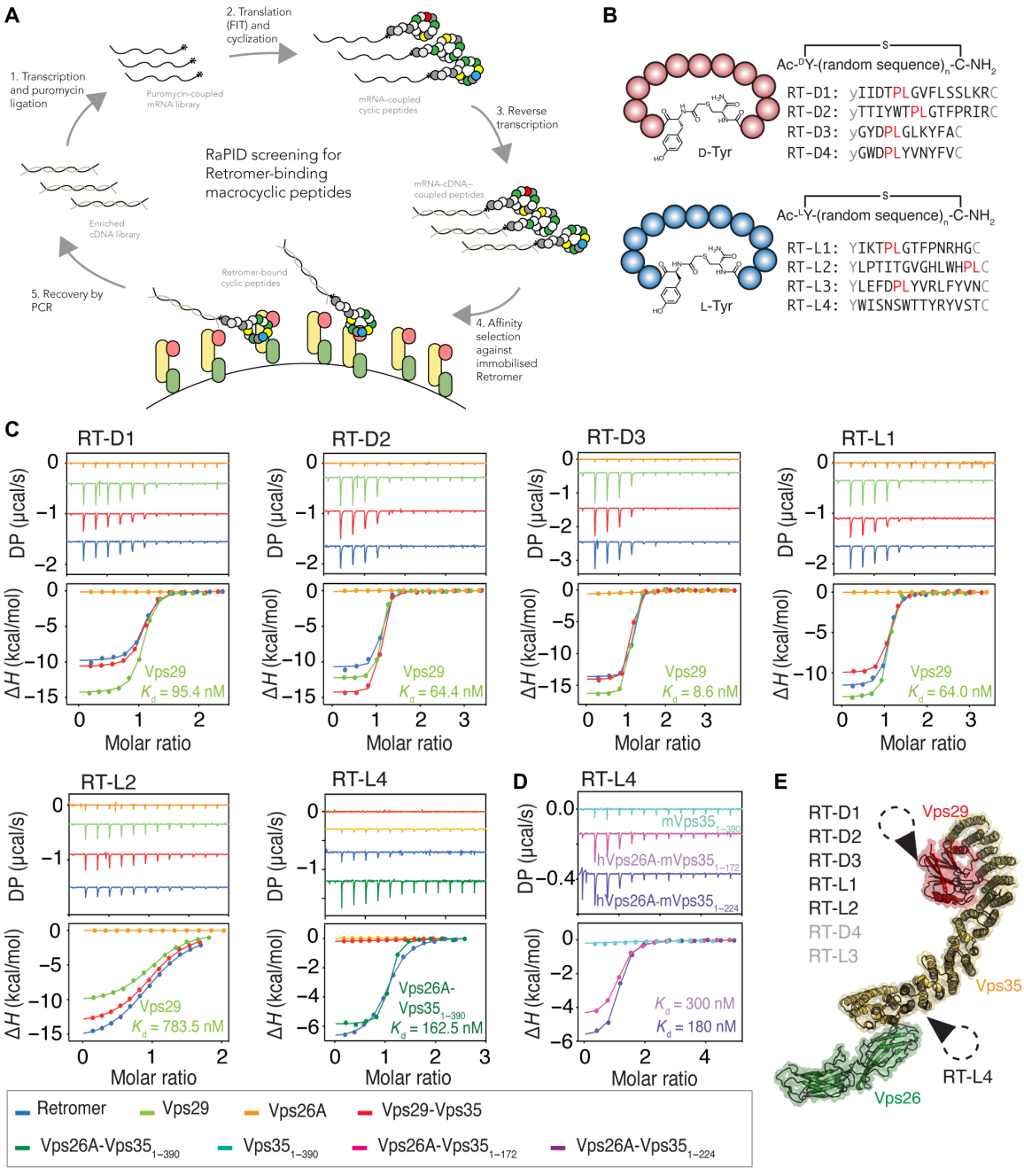

Fig. 1. Cyclic peptides reveal strong binding characteristics with retromer. (**A**) Schematic diagram showing the RaPID system used to screen for cyclic peptides binding to retromer. cDNA, complementary DNA; PCR, polymerase chain reaction. FIT, flexible in vitro translation. (**B**) Eight retromer-binding macrocyclic peptides were identified with either ClAc-D-Tyr or ClAc-L-Tyr as initiating residues. (**C**) Binding of RT-D1, RT-D2, RT-D3, RT-L1, RT-L2, and RT-L4 with retromer (blue), Vps29 (light green), Vps26A (orange), Vps29-Vps35 (red), and Vps26A-Vps35$_{1–390}$ (dark green) by ITC (DP indicates differential power). SPR binding curves for each peptide are shown in fig. S3. (**D**) ITC thermogram showing that addition of α helix 8 and 9 of Vps35 (residues 173 to 224) contributes to RT-L4 binding affinity but is not essential for interaction. All ITC graphs represent the integrated and normalized data fit with 1-to-1 ratio binding. The binding affinity (K_d) is given as means of at least three independent experiments (table S2). (**E**) Relative binding position of each cyclic peptide to retromer based on the ITC measurements indicated on the structure of the mouse retromer complex [Protein Data Bank (PDB) ID: 6VAC] (*61*).

175 to 195) contributes to the binding but is not essential. Overall, we have found that the cyclic peptides RT-D1, RT-D2, RT-D3, RT-L1, and RT-L2 (and likely RT-D4 and RT-L3) bind specifically to Vps29, but RT-L4 binding occurs at the interface between the Vps26A and Vps35 subunits (Fig. 1E).

Macrocyclic peptides bind to Vps29 through a conserved site, mimicking endogenous accessory proteins

To understand the molecular basis of how the discovered macrocyclic peptides bind to retromer, we next cocrystallized Vps29 with RT-D1, RT-D2, RT-D3, RT-L1, and RT-L2. With extensive

crystallization trials, we successfully solved structures of human Vps29 in complex with RT-D1, RT-D2, RT-L1, and RT-L2 (Fig. 2 and table S3). For RT-D3, the complex structure was successfully determined using Vps29 from *C. thermophilum* (ctVps29). In all five complex structures, the conformation of Vps29 is highly similar to apo Vps29 (root mean square deviation ranges from 0.6 to 1.3 Å), with cyclic peptide density clearly visible (Fig. 2A and fig. S3A). Unexpectedly, although the precise details differed for each macrocyclic peptide, they all bound to the same hydrophobic surface groove on Vps29 composed of multiple conserved residues including Leu^{2}, Leu^{25}, Leu^{152}, Tyr^{163}, Tyr^{165}, and Val^{174} (human numbering) (Fig. 2B). This hydrophobic cavity is highly conserved throughout evolution (Fig. 2B) and is located on the opposite surface of Vps29 relative to the Vps35 binding region (Fig. 2C).

Each cyclic peptide adopts a different conformation when bound to Vps29, as expected from their lack of sequence identity (Fig. 2D and fig. S3B). However, a notable feature of all of the Vps29-binding peptides is a Pro-Leu dipeptide motif present in a β-hairpin structure that inserts into the conserved hydrophobic site on Vps29 (Figs. 1B and 2, D and E). Further analysis reveals the residue in front of the Pro-Leu motif (position −1, with the Pro designated as position "0") that is important for stabilizing the β-hairpin–like configuration, forming multiple hydrogen bonds with nearby residues including the side chain hydroxyl group of Vps29 Tyr^{165} (Fig. 2, D and E). Notably, TBC1D5, VARP, and the bacterial hijacking molecule RidL all engage Vps29 at the same site using a similar Pro-Leu dipeptide at their core (Fig. 2F) (*40*, *43*, *44*, *56*, *62*, *63*).

The Vps29-binding peptides that we have identified mimic the interactions of endogenous and bacterial ligands but bind with higher affinity. We assessed the importance of peptide cyclization for this increased affinity using a linear version of RT-D1 and found that this reduced the affinity by approximately sixfold to 0.76 μM (fig. S3C). In addition to the core Pro-Leu dipeptide motif and the cyclic structure, the residues at positions +4 to +7 of the peptides also form extensive contacts with a surface groove composed of Vps29 side chains Val^{172}, Lys^{173}, and Val^{174} (Fig. 2D and fig. S3B). Again, using RT-D1 as an example, we found that mutations of these residues (positions +4, +5, +7, and +8) to alanine significantly reduced the affinity for retromer to ~2.2 μM (fig. S3C). This interaction network is shifted by 8 Å toward Lys^{188} in the ctVps29–RT-D3 structure (equivalent to Arg^{176} in human Vps29), which may explain the weaker binding of ctVps29 to RT-D3 compared to human Vps29 (Fig. 2D and fig. S3D). Another noteworthy observation was found in the Vps29–RT-L1 structure, where a potential secondary cyclic peptide binding pocket was identified, surrounded by helix 3 and Ile^{91} of Vps29 (fig. S3E), a region known to be required for Vps35 binding. In this binding pocket, we found that two RT-L1 peptides are bound to each other, forming extensive contacts with residues located on helix 3 and the adjacent loop region of Vps29 (fig. S3F). This binding of RT-L1 to a secondary site in Vps29 is likely due to a crystallization-induced contact, but it could suggest a potential site for targeting the Vps29-Vps35 interaction in the future.

The RT-L4 macrocyclic peptide is a molecular chaperone that binds to the interface between Vps26A and Vps35

One of our initial goals was to identify potential molecular chaperones that can stabilize the retromer complex; hence, we next assessed the impact of the macrocyclic peptides on the thermal stability of retromer using differential scanning fluorimetry (fig. S4A). The Vps29-binding peptides RT-D1, RT-D2, RT-D3, RT-L1, and RT-L2 all increased the melting temperature (T_m) of Vps29 upon addition of a 20-fold molar excess (fig. S4A), consistent with their high affinities. In contrast, however, none of the Vps29-specific macrocyclic peptides had a significant impact on the thermal stability of the trimeric retromer holo-complex (fig. S4B). This suggests that increasing the thermal stability of Vps29 alone is insufficient to enhance the stability of the entire retromer complex in solution. In contrast, the addition of RT-L4 resulted in a substantial 2° to 6.5°C enhancement in the T_m of the retromer holo-complex in a dose-dependent manner (Fig. 3A and fig. S4, C and D). Similarly, the RT-L4 peptide resulted in an 8°C increase in T_m for the Vps26A-$Vps35_{1–390}$ subcomplex, and, as expected in control experiments, it did not affect the thermal stability of either Vps26A or Vps29 alone (fig. S4C). Using mass photometry, we found that the retromer holo-complex was maintained at its trimeric state upon the addition of cyclic peptides, suggesting that the enhancement in the T_m of the retromer was not the result of high-order oligomer formation (fig. S5A). These results together indicate that RT-L4 stabilizes retromer through its interaction at the interface between Vps26A and Vps35, possibly by acting as a molecular "staple" between the two subunits. In parallel, we also compared the binding and thermal stability effect of RT-L4 against the previously published retromer chaperone R55 and its derivative compound 2a (*20*, *48*). Using ITC, we confirmed that both chaperone R55 and compound 2a bind retromer, but with much lower affinity than RT-L4 (table S4 and fig. S5B). While we observed weak binding, we were unable to detect significant improvement in the T_m of retromer in the presence of either R55 or compound 2a under the same experimental conditions as RT-L4 (fig. S5C). Even in the presence of 1 mM R55 (>300-fold molar excess), little impact on Retromer stability was detectable (fig. S5D), although a second unfolding event was observed that might indicate partial stabilization of the Vps29-Vps35 complex (*20*, *48*). The difference is likely explained by lower binding affinity of both R55 and compound 2a to retromer. Our results thus indicate that RT-L4 can act as a potent molecular stabilizer of retromer in vitro.

Next, we sought to map the exact binding region of RT-L4 to better investigate the mechanism of its interaction and how this results in the enhanced thermal stability of retromer. Using ITC, we found that RT-L4 binds to zRetromer with a K_d of 88 nM, which is highly comparable to human retromer or the Vps26A-$Vps35_{1–390}$ subcomplex (table S2 and fig. S6A). In contrast, RT-L4 binds with lower affinity to ctRetromer with a K_d of 5 μM (table S2 and fig. S6B). As our data indicated that RT-L4 binds to a site that is formed by a combined interface on Vps35-Vps26A, streptavidin agarose beads coated with biotinylated RT-L4 were used to pull down purified Vps26A-$Vps35_{1–390}$, incorporating several specific point mutations, and this revealed that peptide binding was abolished by a D128R mutation in Vps35 (Fig. 3B). The Asp^{128} side chain is part of a conserved surface adjacent to the Vps35-Vps26A interface (Fig. 3C) and makes a minor contact with the extended N terminus of SNX3 when in a ternary complex with the SNX3 adaptor and ΩΦ[LV] sequence containing cargo peptides (where Ω and Φ are aromatic and hydrophobic side chains) (*3*, *59*). In contrast, RT-L4 contains a number of aromatic residues that could potentially contribute to high-affinity binding. Mutation of any of these residues to alanine shows that they are essential for retromer interaction (Fig. 3, D and E). Similarly, the linear form of RT-L4 was unable to bind to retromer (Fig. 3D), suggesting that both aromatic residues and peptide cyclization are critical for the interaction.

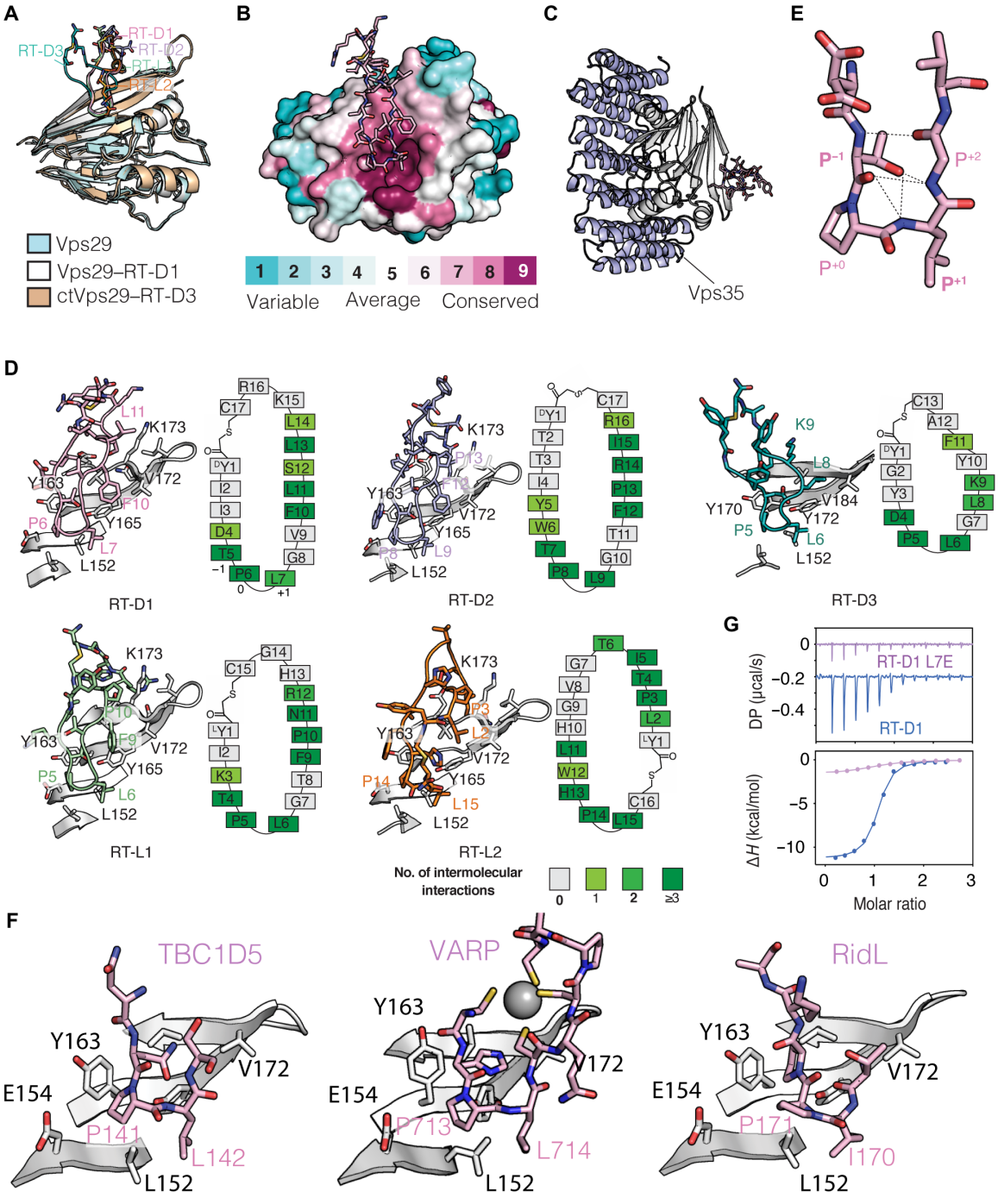

Fig. 2. Crystal structures of Vps29 in complex with cyclic peptides. (**A**) Superimposition of the crystal structures of Vps29 in complex with five macrocyclic peptides. (**B**) Sequence conservation mapped onto the hVPS29 structure surface highlights the conserved binding site for each of the cyclic peptides, with RT-D1 shown as an example. (**C**) Superimposition of the Vps29–RT-D1 peptide complex with the Vps29-Vps35$_{483–780}$ crystal structure (PDB ID: 2R17) (*57*). The cyclic peptides bind opposite to the Vps35 interface. (**D**) Details of macrocyclic peptides in stick representation bound to Vps29. Schematic diagrams indicate the number of intermolecular contacts (salt bridge, hydrogen bonds, and hydrophobic interactions) of each residue on the peptide with Vps29. The residues on the peptide with 0, 1, 2 and ≥3 contacts are shown in gray, light green, green, and dark green boxes, respectively. Each peptide uses a core Pro-Leu sequence forming a β-hairpin, labeled as position 0 and 1 for reference. Electron density for each peptide is shown in fig. S3. (**E**) Close-up of the β-hairpin conformation of the bound RT-D1 peptide. (**F**) TBC1D5 (PDB ID: 5GTU) (*56*), VARP (PDB ID: 6TL0) (*63*), and RidL (PDB ID: 5OSH) (*43*) bind to the same site of Vps29 using a similar β-hairpin composed of a Pro-Leu dipeptide sequence. For clarity, only the key residues involved in the contact are shown. (**G**) ITC thermogram for the titration of RT-D1 (purple) and RT-D1 L7E (blue) with retromer showing the importance of Pro-Leu motif in the interaction. The graph represents the integrated and normalized data fit with a 1-to-1 binding ratio.

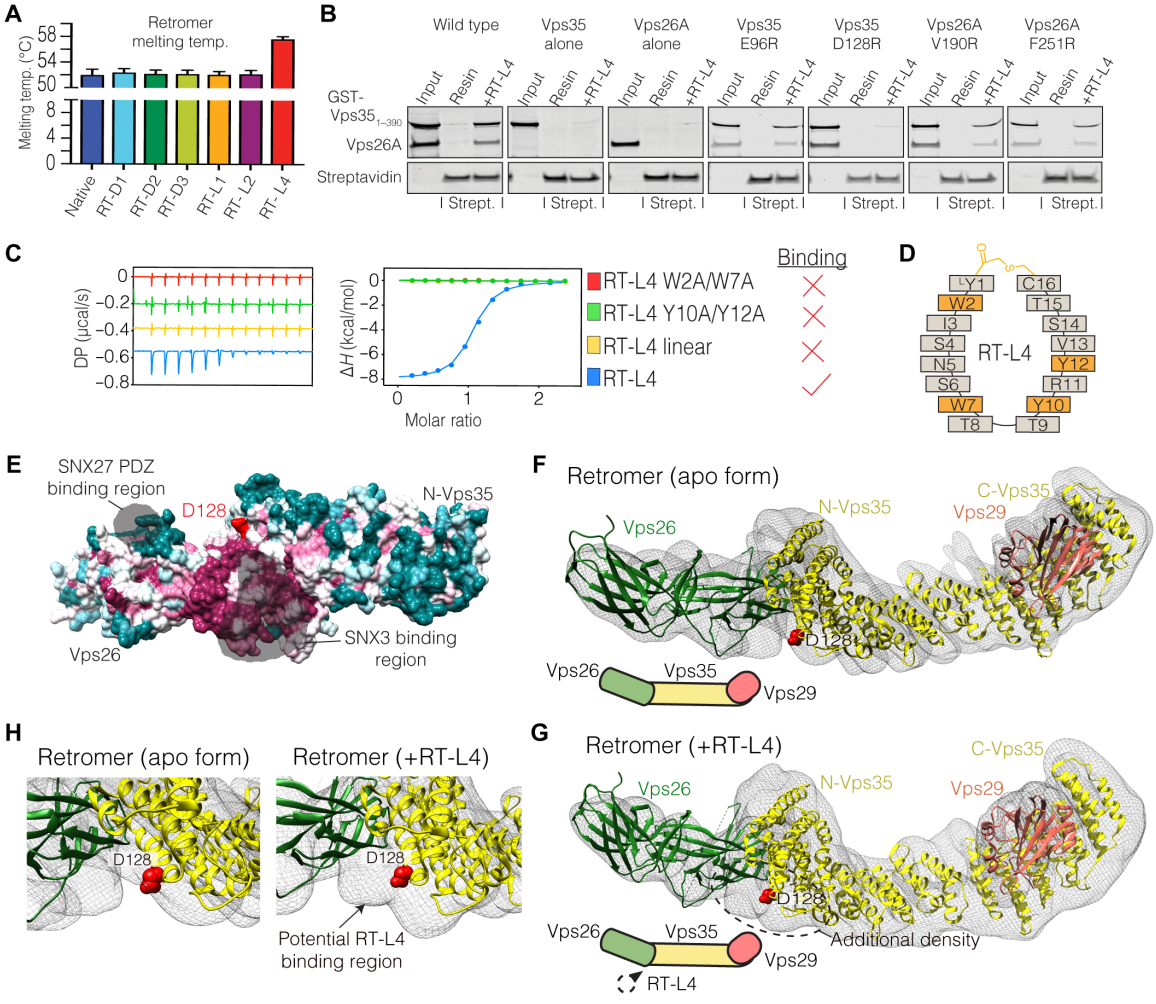

Fig. 3. The RT-L4 macrocylic peptide is a molecular chaperone that binds retromer at the Vps35-Vps26 interface. (**A**) Bar graph summarizing the measured thermal unfolding temperatures (T_m) of retromer in the presence of cyclic peptides. Raw data are shown in fig. S4. (**B**) Pull-down assay showing the interaction of biotinylated RT-L4 bound to streptavidin-coated agarose beads with either wild-type Vps26A-Vps35$_{1–390}$ subcomplex or indicated point mutants. Individual Vps26A and Vps35$_{1–390}$ proteins do not bind the peptide, while the D128R mutation in Vps35$_{1–390}$ specifically blocks subcomplex interaction. (**C**) Sequence conservation map of Vps26A-Vps35$_{12–470}$ subcomplex (PDB ID: 5F0L) highlighting the proposed RT-L4 binding site and its relationship to known binding sites for SNX3 (*59*) and SNX27 (*65*). (**D**) ITC thermograms showing that linear RT-L4 or RT-L4 with alterations in bulky aromatic side chains is unable to bind to retromer. The graph represents the integrated and normalized data fit with a 1-to-1 binding ratio. (**E**) Schematic diagram of RT-L4 highlighting aromatic residues important for binding to retromer. (**F**) Cryo-EM reconstruction of the human retromer (apo form) and (**G**) in complex with RT-L4. Cryo-EM density is shown as a transparent molecular envelope, with crystal structures of retromer subcomplexes (PDB IDs: 2R17 and 5F0L) overlapped to the map (contoured at 4.7σ). The additional density seen on addition of the cyclic peptide added retromer supports the mutagenesis data indicating that RT-L4 binds at the Vps26 and Vps35 interface. (**H**) Enlarged view of the Vps26 and Vps35 interface highlighting the additional density in the cryo-EM map of RT-L4–added retromer but not in the apo form. For clarity, D128 of Vps35 is highlighted in red. DMSO, dimethyl sulfoxide.

With the multiple attempts to cocrystallize RT-L4 without success, we further explored the site where RT-L4 binds retromer using single-particle cryo–electron microscopy (cryo-EM). In previous work, wild-type retromer was found to form a mixed population of heterotrimers and multiple higher-order oligomers in vitreous ice, so we used an established mutant called "3KE retromer" (point mutations E615A/D616A/E617A in Vps35) that favors the heterotrimeric species over higher-order oligomers for our analyses (*61*). We determined structures of both apo- and RT-L4–bound 3KE retromer under the same conditions to ascertain whether the RT-L4 binding site could be identified (Fig. 3, F to H; fig. S6, C to F; and table S5). At the current resolution, we detected no structural differences between wild-type heterotrimer (*61*) and the 3KE mutant. Comparison of our reconstructions indicates that there is additional density at the Vps26-Vps35 interface in the presence of the RT-L4 peptide, although the estimated resolution of apo and RT-L4/retromer structures (~5.9 Å; 0.143 Fourier Shell Correction (FSC) cutoff in RELION) is too low to unambiguously assign peptide density (Fig. 3, F to H, and fig. S6, C and D). Overall, our cryo-EM data show that there are no gross structural changes in retromer induced by the RT-L4 peptide, and, although not conclusive, these reconstructions provide support for our biophysical and mutagenesis data, indicating that RT-L4 binds and stabilizes retromer at the Vps26/Vps35 interface. Higher-resolution data will be required, however, to unambiguously identify

specific residues in both retromer and the peptide that mediate the interaction.

The impact of cyclic peptides on the interactions between retromer and known regulatory proteins

Given the high affinity and specificity of the macrocyclic peptides for retromer, it was critical to assess their potential effects on retromer's interaction with essential regulatory, accessory, and adaptor proteins. We used RT-L4, with its distinct affinity for the Vps26-Vps35 complex, and RT-D3 as a representative Vps29-binding peptide and tested retromer binding proteins for which binding mechanisms were known including TBC1D5 (*56*), SNX3 (*59*), Fam21 (*64*), SNX27 (*65*), and the bacterial hijacking molecule RidL (*40*, *43*, *44*) (Fig. 4, A to E, and fig. S7A). Glutathione *S*-transferase (GST)–tagged TBC domain of human TBC1D5 ($TBC1D5_{TBC}$) bound retromer in pulldowns, and this interaction was inhibited by addition of RT-D3 as expected on the basis of their overlapping binding site (Fig. 4A). A similar result was observed using ITC, where we observed binding between $TBC1D5_{TBC}$ and retromer with a K_d of 370 nM [consistent with previous reports (*56*)], while binding was undetectable in the presence of competing RT-D3 (Fig. 4B and table S6). The same inhibitory effect was also observed for the N-terminal region of the bacterial effector RidL ($RidL_{1–236}$) (fig. S7A). In contrast, while the addition of RT-D3 blocked retromer from interacting with $TBC1D5_{TBC}$ or RidL as would be predicted from their overlapping binding sites, it had no impact on retromer binding to either SNX27 or SNX3, as assessed in pulldowns and ITC experiments (Fig. 4, A, C, and D). Note that, for ITC and pull-down experiments with SNX3, we found that it was necessary to include a synthetic peptide corresponding to $DMT1\text{-}II_{550–568}$ containing a ΩΦ[LV] cargo motif (where Ω is an aromatic side chain and Φ is a hydrophobic side chain) (*59*). In the absence of this peptide, we could not detect binding of SNX3 to retromer, likely because SNX3 and cargo motifs form a codependent binding interface with the retromer complex (*3*, *59*). To our surprise, the addition of RT-D3 modestly affected retromer binding to Fam21 C-terminal leucine-phenylalanine-acidic (LFa) repeats 19 to 21 (Fig. 4, A and E), a sequence known to associate with a C-terminal region of Vps35 (*22*, *64*). It is therefore likely that Vps29 contributes partially to the binding of LFa sequences of Fam21 as previously reported (*66*) and RT-D3 either directly competes with Fam21 or allosterically affects the Fam21 binding site. These results were further validated using qualitative pulldowns from HeLa cell lysates with biotinylated RT-D3 peptide, where specific loss of TBC1D5 and VARP binding was seen, without any effect on the association of other retromer ligands SNX27, Fam21, SNX3, and SNX27 (Fig. 4F). Together, our data indicate that RT-D3 can specifically inhibit binding to TBC1D5 and, most likely, will also compete with other proteins such as VARP and RidL that bind to the same conserved hydrophobic cavity on Vps29.

In contrast to RT-D3, we found that the RT-L4 peptide had little negative impact on the interaction of retromer with any ligands tested. In GST pulldowns using purified proteins or using biotinylated peptides and HeLa lysates, retromer was able to interact with TBC1D5, VARP, Fam21, SNX27, and the SNX3–DMT1-II complex in the presence of RT-L4 (Fig. 4, A and E). By ITC, we found that the affinity and enthalpy of binding between retromer for either $SNX27_{PDZ}$, $TBC1D5_{TBC}$, or $Fam21_{R19–R21}$ were substantially improved by the addition of RT-L4 (Fig. 4, B, D, and E; fig. S7B; and table S6). The enhancement of retromer binding to $TBC1D5_{TBC}$ by RT-L4 also led to a slight improvement of guanosine triphosphatase (GTPase) activating protein (GAP)–stimulated guanosine triphosphate (GTP) hydrolysis of Rab7a (fig. S7, C and D). In the case of SNX27, the binding between $SNX27_{PDZ}$ and PDZ-dependent cargo peptide, $PTHR_{586–593}$, was also further improved to a K_d of 700 nM by the presence of RT-L4 (Fig. 4G). This suggests that the stabilization of retromer by RT-L4 may be able to enhance binding to some of its key partners, promote GAP activity, and possibly also improve cargo recognition. However, we did observe a modest reduction in the binding affinity of retromer for the SNX3–DMT1-II complex from 154 to 230 μM in the presence of RT-L4 (Fig. 4C and table S6). We speculate that there may be a small degree of overlap between the binding site for RT-L4 and the first part of the N-terminal loop of SNX3, although not enough to markedly perturb the interaction. Given this subtle change, however, we then asked whether the peptide would perturb the interactions between retromer and SNX3 in the presence of a lipid membrane. To do this, we performed a liposome binding assay, where we fused a palmitoylated fatty acid to the N terminus of a cargo peptide. For these experiments, we used a sequence derived from the CI-MPR ($CI\text{-}MPR_{2347–2376}$) and allowed it to insert into liposomes composed of Folch I lipids supplemented with the SNX3-binding phosphatidylinositol-3-phosphate (PtdIns3*P*) (Fig. 4H and fig. S7, E and F). In our control experiments, we found that SNX3 alone was capable of binding Folch I–PtdIns3*P* liposomes both in the presence and absence of cargo peptide. In contrast, retromer only bound stably to PtdIns3*P*-containing liposomes when both SNX3 and cargo peptides were added, similar to previous studies (*67*). In the presence of RT-L4, we observed a subtle reduction of retromer binding to SNX3–CI-MPR cargo-PtdIns3*P* liposomes, consistent with the slightly lower affinity observed by ITC (fig. S7G). In summary, peptides binding to Vps29 have a strong and specific impact on a subset of retromer-associated proteins including TBC1D5 and VARP, without affecting interactions that occur near the Vps35-Vps26 interface (Fig. 4I). The stabilizing RT-L4 peptide does not prevent binding of any known ligands (Fig. 4I), which is an important property of a potential molecular chaperone, although it does have subtle effects on these interactions depending on their respective binding sites.

RT-L4 reveals an unexpected autoinhibitory role for the C-terminal disordered tails of Vps26A and Vps26B

During our analyses of RT-L4, we noted that it showed a lower binding affinity for the paralogous Vps26B-$Vps35_{1–390}$ subcomplex when compared to Vps26A-$Vps35_{1–390}$ (Fig. 5A and table S2). According to the sequence alignment of Vps26, the residues responsible for Vps35 interaction are highly conserved (fig. S8, A and B), while the extended C-terminal tails (residues 298 to 327 in Vps26A) are highly divergent apart from the QRF/YE motif (Fig. 5B and fig. S8A). Notably, when the disordered C-terminal domains of either Vps26A or Vps26B are removed (Vps26AΔC and Vps26BΔC, respectively), the binding affinity for RT-L4 is increased to ~40 nM K_d and is now identical for both subcomplexes (Fig. 5A). We also find a similar improved affinity of RT-L4 for *C. thermophilum* retromer when the tail of Vps26 is removed (fig. S9). This shows that the C-terminal tails of Vps26A and Vps26B have an autoinhibitory effect on binding to RT-L4, with the Vps26B C terminus more strongly inhibiting the interaction.

Given that the RT-L4 peptide also subtly affects binding of retromer to SNX3 and cargos, we were interested to determine whether the

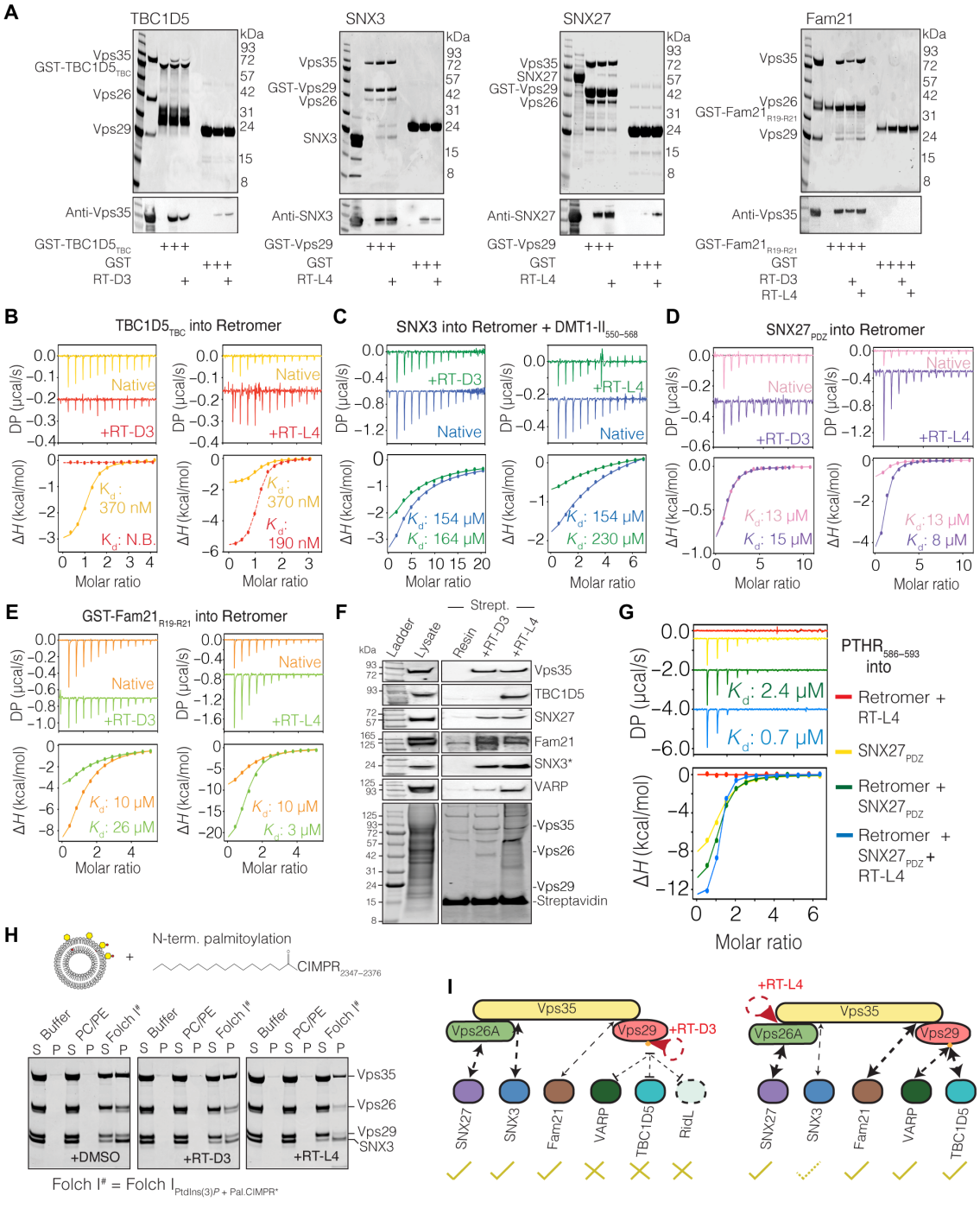

Fig. 4. The effect of cyclic peptides on the interaction of retromer with known regulatory and adaptor proteins. (**A**) Interactions of retromer with TBC1D5, SNX3, SNX27, and Fam21 in the presence of either RT-D3 or RT-L4. GST-TBC1D5$_{TBC}$ and GST-Fam21$_{R19-R21}$ were used as baits for retromer, while GST-tagged retromer (Vps29 subunit) was used as bait for SNX3 and SNX27. (**B**) ITC measurement of TBC1D5$_{TBC}$, (**C**) SNX3 (with DMT1-II$_{550–568}$ present), (**D**) SNX27$_{PDZ}$, and (**E**) GST-Fam21$_{R19-R21}$ with retromer in the presence or absence of RT-D3 or RT-L4. (**F**) Hela cell lysates were incubated with streptavidin agarose coated with biotinylated RT-D3 or RT-L4 and bound proteins subjected to SDS–polyacrylamide gel electrophoresis (PAGE) and Western blotting with antibodies against indicated proteins. (**G**) ITC measurement of PTHR$_{586–593}$ cargo peptide (*97*) with SNX27$_{PDZ}$ alone (yellow), retromer + RT-L4 (red), retromer + SNX27$_{PDZ}$ (green), and retromer + SNX27$_{PDZ}$ + RT-L4 (blue). RT-L4 allosterically enhances the affinity of retromer + SNX27$_{PDZ}$ for cargo. The cargo peptide binds to SNX27. All ITC graphs represent the integrated and normalized data fit with a 1-to-1 binding ratio. The binding affinity (K_d) is given as means of at least two independent experiments. (**H**) Liposome binding assay of retromer with membrane-associated SNX3-cargo complex in the presence of cyclic peptides. Multilamellar vesicles were composed of either control PC/PE lipids or Folch I lipids containing added PtdIns(3)*P* and N-terminal palmitoylated CI-MPR$_{2347–2376}$ peptide (schematic diagram on top). "S" and "P" indicate unbound supernatant and bound pellet, respectively. Control experiments are shown in fig. S7 (B and C). (**I**) Schematic summarizing the effects of RT-D3 and RT-L4 on retromer engagement with known regulatory, adaptor, and bacterial effector proteins.

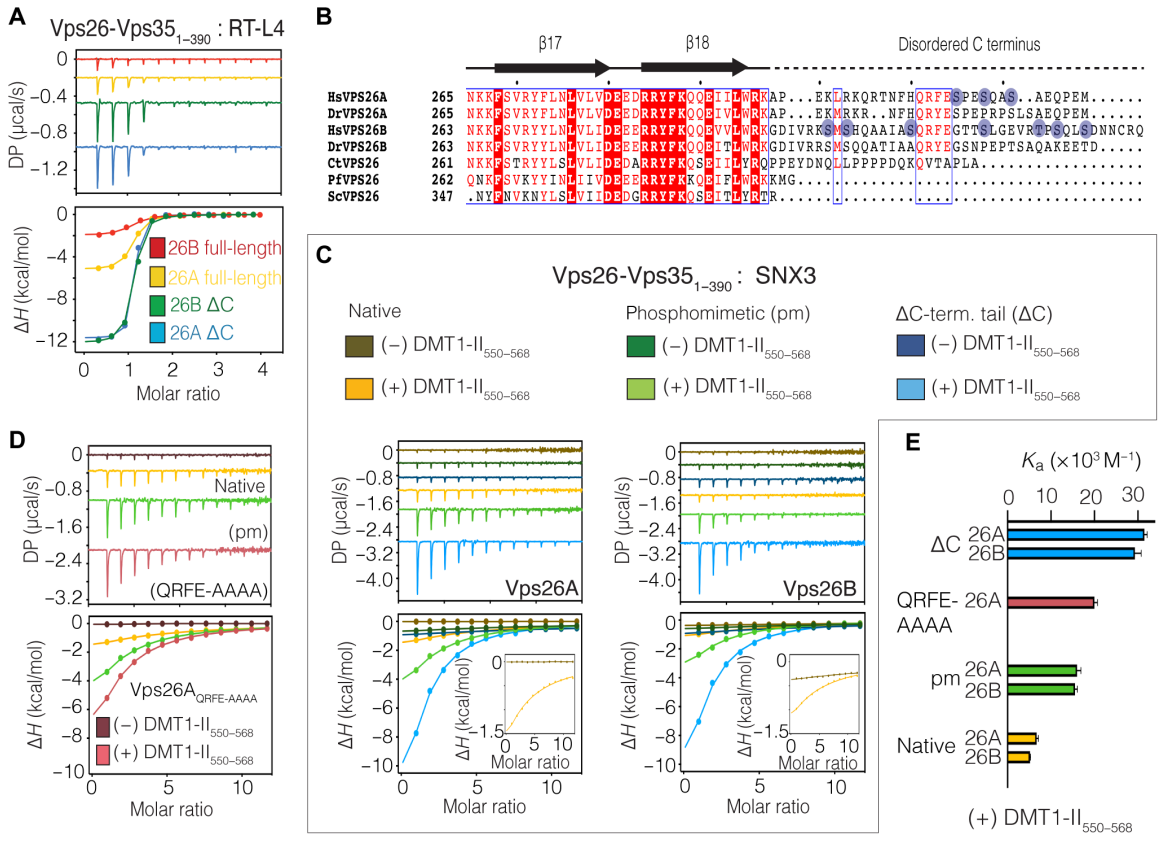

Fig. 5. An autoinhibitory role for the disordered C-terminal tail of Vps26 in binding RT-L4 and SNX3. (**A**) ITC thermogram for the titration of RT-L4 with Vps35$_{1–390}$ subcomplex with either full-length or C-terminal–truncated Vps26A and Vps26B paralogs. (**B**) Sequence alignment of the C-terminal region of Vps26 highlighting the low-sequence similarity of the unstructured C-terminal tail apart from the QRF/YE motif highlighted with a blue box. Sites of phosphorylation are indicated in circle (www.phosphosite.org) (*68*). Hs, *Homo sapiens*; Dr, *D. rerio*; Ct, *C. thermophilum*; Pf, *Plasmodium falciparum*; Sc, *Saccharomyces cerevisiae*. (**C**) ITC measurement of SNX3 binding to native, phosphomimetic (pm), and C-terminal tail–truncated (ΔC) versions of Vps26A/B-Vps35$_{1–390}$ subcomplexes. In each case, the presence of DMT1-II cargo peptide was required to detect SNX3 binding. (**D**) ITC measurement of SNX3 binding to QRFE-AAAA mutant Vps26A-Vps35$_{1–390}$. ITC thermograms in (A), (C), and (D) represent the integrated and normalized data fit with a 1-to-1 binding ratio. (**E**) Summary of binding affinities of SNX3 for each Vps26A/B-Vps35$_{1–390}$ subcomplex in the presence of DMT1-II$_{550–568}$ cargo peptide. For clarity, the association constant (K_a) is shown. The binding affinity is given as means of at least two independent experiments.

C-terminal tails of Vps26 might also influence SNX3 interactions. Intriguingly, SNX3 (in the presence of DMT1-II cargo) binds to Vps26AΔC-Vps35$_{1–390}$ with a significantly increased affinity compared to full-length Vps26A-Vps35$_{1–390}$ (Fig. 5C and table S7). This suggests that there is a self-association of the C-terminal tail that weakens the SNX3-cargo interaction. Previous proteomics have shown that the C-terminal disordered sequences of human and mouse Vps26A and Vps26B can be phosphorylated, although the role of these posttranslational modifications and their regulation have not been studied (Fig. 5B) (*68*). We engineered a Vps26A variant with three phosphomimetic mutations in its C-terminal tail and tested the affinity of the Vps35$_{1–390}$/Vps26A phosphomimic complex for SNX3 in the presence of DMT1-II by ITC (Fig. 5C). This mutant showed an enhanced affinity to the cargo-adaptor complex, although not to quite the extent of the complete removal of the Vps26A tail. Similar enhancement of binding to the SNX3 cargo-adaptor complex was also observed when we mutated the conserved QRFE motif of Vps26A to polyalanine (Fig. 5, D and E). Our data suggest that the tails of Vps26A and Vps26B play an unexpected autoinhibitory role in the interaction of retromer with the SNX3 adaptor and associated cargos such as DMT1-II and CI-MPR in vitro, and, potentially, phosphorylation of these tails could enhance SNX3-cargo interactions. The observation that Vps26B is more strongly autoinhibited than Vps26A might explain previous studies showing that the CI-MPR can only bind to Retromer containing Vps26B with the tail removed (*69*). However, this will require further studies of their interactions in situ to be confirmed.

Macrocyclic peptides as molecular probes to study retromer-mediated endosomal trafficking

With established mechanisms of binding in vitro, we sought to assess the basic utility of these macrocyclic peptides as novel molecular tools for the study of retromer. In the first instance, we examined their use as fluorescent probes of retromer localization in cells (Fig. 6). As the peptides were not membrane permeable for cellular uptake, we used a reversible cell permeabilization approach with the pore-forming bacterial toxin streptolysin O (SLO) (*70*). After permeabilization, cells were treated with fluorescein isothiocyanate (FITC)–labeled RT-D3 and RT-L4 and then processed for imaging and colabeling with specific endosomal markers. In the absence of SLO permeabilization, no intracellular fluorescence was detected for the FITC-labeled peptides, indicating that they are not crossing

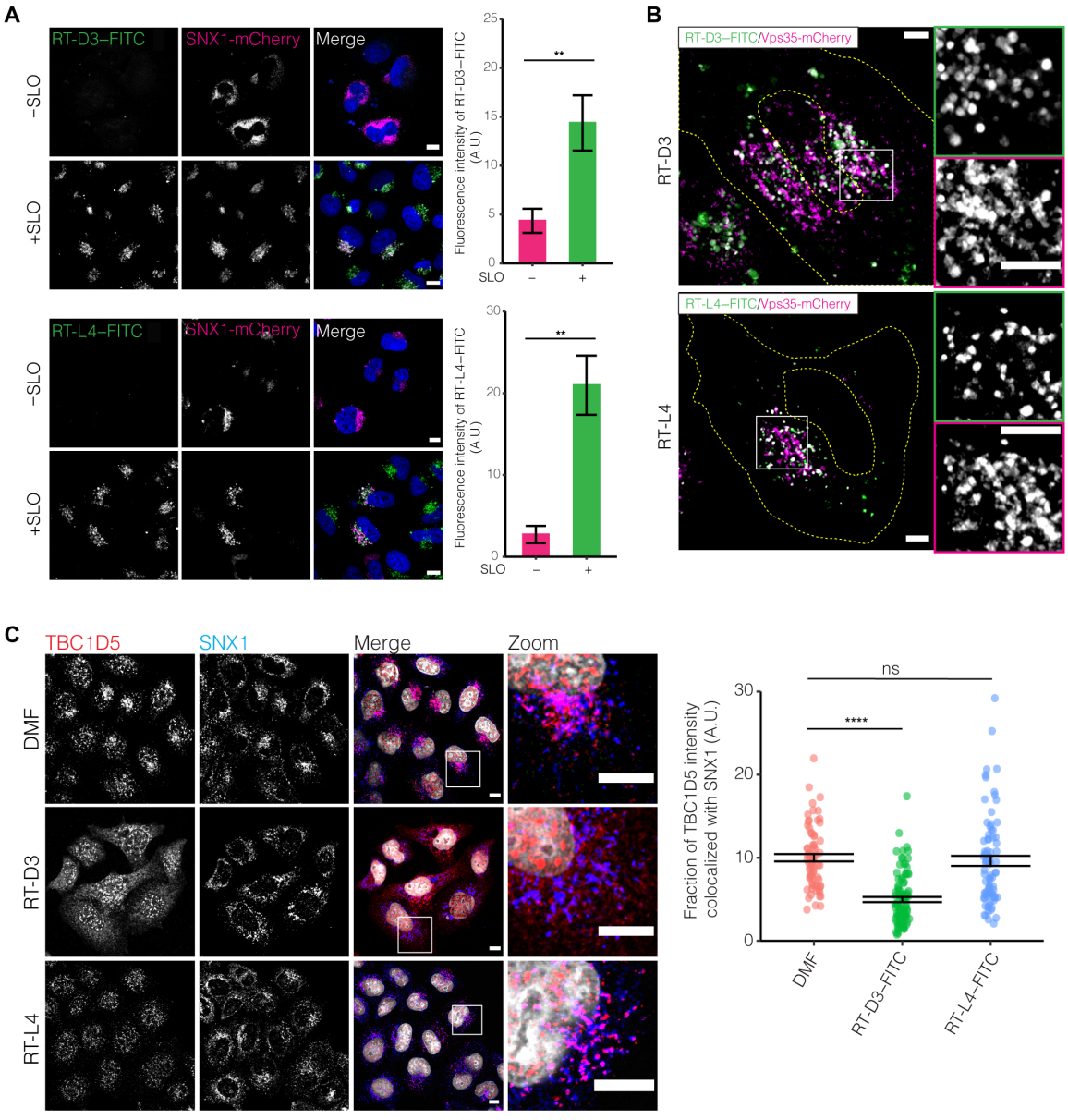

Fig. 6. Macrocyclic peptides can be used to study retromer localization in cells. (**A**) Specific targeting of endosomal structures by SLO-delivered cyclic peptides. HeLa cells transiently expressing SNX1-mCherry were exposed to SLO at 37°C for 9 min before incubating with the cyclic peptide RT-D3–FITC or RT-L4–FITC on ice for 5 min. Permeabilized cells were recovered in the recovery medium containing Hoechst 33342 for 20 min and then fixed in 4% paraformaldehyde (PFA). The negative control (−SLO) shows no labeling of intracellular structures. Scale bars, 10 μm. Graphs show the fluorescence intensity of RT-D3–FITC or RT-L4–FITC in HeLa cells (means ± SEM). Two-tailed Student's *t* test was used to determine the statistical significance ($n = 3$). $^{**}P < 0.01$. A.U., arbitrary units. (**B**) HeLa cells transiently expressing Vps35-mCherry were labeled by SLO-delivered cyclic peptide RT-D3–FITC or RT-L4–FITC, fixed in 4% PFA, and imaged by Airyscan superresolution microscopy. Scale bars, 5 μm. (**C**) HeLa cells treated with SLO-delivered RT-D3–FITC, RT-L4–FITC, or *N*,*N*′-dimethylformamide (DMF) control were incubated in recovery medium for 2 hours, fixed in ice-cold methanol, and coimmunolabeled with antibodies against endogenous TBC1D5 and SNX1, followed by Alexa Fluor–conjugated fluorescent secondary antibodies. Scale bars, 10 μm. The colocalization between TBC1D5 and SNX1 was quantified by Pearson's correlation coefficient and was represented in the graph (means ± SEM). Two-tailed Student's *t* test was used to determine the statistical significance ($n = 3$). $^{****}P < 0.0001$; ns, not significant.

the membrane or being nonspecifically internalized into the lumen of endosomal compartments (Fig. 6A). In permeabilized cells, however, both FITC-labeled RT-D3 and RT-L4 were recruited to endosomal structures labeled with SNX1 (Fig. 6A). Using Airyscan superresolution microscopy, we found that the peptides also colabeled endosomal structures marked with mCherry-tagged Vps35 (Fig. 6B). Last, we examined the impact of the peptides on the endosomal recruitment of TBC1D5, which has previously been shown to depend on interaction with retromer (*40*, *43*, *44*, *56*, *71*). As expected, addition of unlabeled RT-L4 had no discernible effect on TBC1D5 localization; however, RT-D3, which binds to the same site on Vps29 as TBC1D5, caused significant dispersal of TBC1D5 from endosomal structures

(Fig. 6C). In orthogonal experiments, we adapted an electroporation approach to deliver peptides to cells (*72*) and observed a similar inhibition of retromer-dependent TBC1D5 localization using electroporation (fig. S10). Overall, our data suggest that the retromer-binding macrocyclic peptides are capable of acting as molecular probes for retromer localization.

DISCUSSION

De novo macrocyclic peptides that target the retromer endosomal trafficking complex

In this work, the versatile RaPID screen was used to identify a series of potent retromer-targeting macrocyclic peptides. These bind with high affinity and specificity to retromer using two distinct evolutionarily conserved binding sites on either Vps29 or at the interface between Vps26 and Vps35. The cyclic peptides in the inhibitor subgroup (RT-D1, RT-D2, RT-D3, RT-L1, and RT-L2) reveal strong binding through the highly conserved surface groove of Vps29, lying on the opposite surface to that bound by the Vps35 subunit. Detailed structural analyses showed that these cyclic peptide inhibitors all form a β-hairpin configuration with a core Pro-Leu motif. These Vps29-binding cyclic peptides are effective at blocking association with TBC1D5, VARP, and the bacterial hijacking molecule RidL, which are known to bind the same site using a similar β-hairpin structure (*40*, *43*, *44*). It is intriguing that all the Vps29-binding peptides have been selected for the presence of this Pro-Leu dipeptide and that this peptide has also evolved to mediate binding of endogenous ligands of the retromer complex such as TBC1D5, VARP, and RidL. The de novo macrocyclic peptide screening has therefore inadvertently identified an evolutionarily conserved binding mechanism, and previous screens of Bromodomain and Extra-Terminal (BET) domain–binding peptides also uncovered sequence preferences that partly mimicked known endogenous ligands (*73*). Given that Vps29 is also a component of the retriever complex, a Retromer-related assembly containing homologous subunits Vps35L and Vps26C (*74*, *75*), these cyclic peptide inhibitors may also provide tools for studies of retriever. However, known retromer interactors such as TBC1D5 or VARP that depend on Vps29 for association have not been detected in retriever interactomes (*74*), so whether the same binding site in Vps29 is accessible within the retriever complex remains to be confirmed.

Among the identified macrocyclic peptides, RT-L4 binds specifically to the interface between the N-terminal domain of Vps35 and the C-terminal subdomain of Vps26 and is the sole molecule to show a significant ability to stabilize the retromer complex. In the recent cryo-EM structure of mammalian retromer, it was found that Vps26 and the N-terminal portion of Vps35 exhibit substantial flexibility compared with other regions of the complex (*61*). We speculate that the improved thermal stability of retromer in the presence of RT-L4 may be partly due to reduced flexibility in these two subunits. The RT-L4 peptide did not inhibit the binding of retromer to its essential interacting partners including SNX27, Fam21, TBC1D5, and VARP and in fact led to a general increase in their binding affinity in vitro. RT-L4 did have a minor effect however on binding of retromer to SNX3 and ΩΦ[LV] motif-containing cargo, consistent with the fact that the RT-L4 binding site partially overlaps with the site where the N-terminal disordered domain of SNX3 engages Vps26 and Vps35 (*59*). Certainly, the impact of RT-L4 on the ability of the retromer to form the membrane-associated arches with SNX3 and ΩΦ[LV] motif–containing cargo (*76*) will need to be tested.

Macrocyclic peptides as molecular tools for the study of retromer function

The series of macrocyclic peptides found here provide novel molecular probes for the study of retromer and endosomal trafficking. First, using a simple reversible permeabilization approach, we have successfully delivered the cyclic peptides RT-D3 and RT-L4 into cells and find that they are specifically targeted to the retromer-positive endosomal structures. Thus, the peptides can be used to examine endogenous retromer localization in situ and could feasibly be used to study retromer in live cells or using superresolution approaches with different types of fluorescent dyes apart from the simple FITC labeling strategy used here. The RT-D3 peptide also affects recruitment of proteins such as TBC1D5 that depend on binding to the Vps29 subunit of the complex, and therefore could be used to probe the impact of acutely disrupting this interaction in the future. In addition to studying the localization of retromer, the RT-L4 peptide provided a highly specific substrate for purification of the retromer complex from cells and, in the future, could be useful for proteomic studies of retromer in diverse cells, tissues, and organisms. We also envisage that these peptides will provide tools for enhancing retromer stability for future structural studies of its interactions with accessory and regulatory proteins by cryo-EM and x-ray crystallography.

Our studies of the RT-L4 peptide binding to the Vps26-Vps35 interface revealed an autoinhibitory role for the C terminus of the Vps26A and Vps26B paralogs. Removal of their divergent C-terminal tails significantly increased the affinity of both retromer complexes for the RT-L4 peptide to similar levels, leading us to then test the impact of the Vps26A and Vps26B tail domains on binding to the SNX3–DMT1-II cargo-adaptor complex, a native ligand that engages Retromer at a similar location. Again, removal of the C-terminal disordered domains significantly improved the affinity of retromer for SNX3–DMT1-II, confirming that their autoinhibitory activity has a functional importance. Furthermore, this may be regulated by phosphorylation of the Vps26A and Vps26B tails, as phosphomimetic mutants have a higher affinity for SNX3–DMT1-II than the wild-type proteins. Since the discovery of the Vps26B paralog of Vps26A, it was clear that the most significant difference between the two proteins was the sequence of their C-terminal domains (*77*, *78*). Later, it was shown that Vps26A but not Vps26B retromer bound to the SNX3-dependent cargo CI-MPR; however, CI-MPR binding and trafficking by Vps26B were restored when its tail was deleted (*69*). Our data demonstrate a direct role for both the Vps26A and Vps26B tails in negatively regulating the binding of SNX3-cargo in vitro, with the Vps26B tail having a more potent autoinhibitory sequence than that of Vps26A. This suggests that an activating switch such as phosphorylation of Vps26 proteins or binding of another regulatory protein may promote the recruitment of SNX3-cargo complexes by retromer in cells, although the specific nature of this switch remains to be determined.

Toward therapeutic targeting of retromer

Endolysosomal trafficking and regulation of proteostasis is emerging as an attractive target in the treatment of a range of diseases, including neurodegenerative disorders such as AD and PD, infection by viral and bacterial pathogens, and other diseases affected by defective endosomal signaling such as cancer. There is an increasing interest in developing molecules for both inhibition and enhancement of retromer activity in these processes (*11*, *79*, *80*). As shown previously, peptides that target retromer and compete with

the viral L2 protein can reduce HPV infection in cell and animal models (*38*, *45*, *81*), while a small molecule with retromer chaperoning activity can reduce cellular accumulation of toxic material causing neurodegeneration (*33*, *46*–*51*, *82*–*86*). However, these peptides and small molecules have only a relatively low affinity for retromer, and their specificities and pharmacological profiles are essentially unknown.

Because of their typically high affinity and larger surface area coverage, macrocyclic peptides are emerging as an important class of molecules for the design of new drugs and molecular probes targeting proteins and protein-protein interactions, often considered difficult using traditional small-molecule approaches (*54*, *87*–*90*). The peptides that we have found can be classified as either retromer inhibitors or stabilizers, and we provide a comprehensive biochemical and structural explanation for how each cyclic peptide associates with retromer and affects its native molecular interactions. The retromer inhibitors that we identified were able to potently block TBC1D5, VARP, and bacterial effector RidL binding, suggesting that this conserved site in retromer is primed for targeting by peptide- or small molecule–based inhibition. The stabilizing peptide RT-L4 enhanced retromer association with known regulatory proteins. In particular, the enhancement of binding between retromer and Fam21 of the WASH complex by RT-L4 suggests the potential use of RT-L4 to rescue the binding caused by the PD-linked Vps35 D620N mutant. The RT-L4 peptide has much higher affinity and capacity to stabilize retromer in vitro compared to the previously reported small-molecule chaperones R55 (*48*) and its derivative compound 2a (*20*). This highlights the potential of targeting the Vps26 and Vps35 interface for the design of novel pharmacological chaperones of retromer in future studies. While the macrocyclic peptides described here are potential leads for therapeutic targeting of retromer, notable hurdles will include cell permeability, oral availability, and an ability to cross the blood-brain barrier when targeting neurological diseases. However, new approaches show promise in overcoming these barriers, including the use of nonstandard amino acids with novel activities and solubility profiles, coupling to various cell-targeting peptides, and novel delivery methods (*90*–*93*). Alternatively, the peptides found here could provide the basis for competitive screening for drug-like molecules that target the same binding sites.

In summary, we have identified a series of retromer-targeting macrocyclic peptides and demonstrate their potential for retromer inhibition and activation on the basis of a comprehensive understanding of their different mechanisms of action. They will be a valuable resource for the study of retromer function at the cellular and molecular levels and represent promising leads for the targeting of retromer in a variety of diseases caused by dysregulation or disruption of the endosomal membrane trafficking system.

MATERIALS AND METHODS

Chemicals and antibodies

Rabbit polyclonal anti-TBC1D5 was purchased from Proteintech (17078-1-AP). Goat polyclonal TBC1D5 antibody was from Santa Cruz Biotechnology (sc-99661). Mouse monoclonal anti-SNX1 was purchased from BD Transduction Laboratories (611483). Rabbit polyclonal Vps26A antibody was from Abcam (ab23892). Mouse monoclonal anti–α-tubulin (clone DM1A; T9026) was purchased from Sigma-Aldrich. Goat polyclonal anti-Vps35 (NB100-1397) was purchased from Novus Biologicals. Secondary donkey anti-mouse immunoglobulin G (IgG) Alexa Fluor 647 (A31571) and donkey anti-rabbit IgG Alexa Fluor 555 (A31572) were purchased from Thermo Fisher Scientific. The linear peptides DMT1-II$_{550–568}$ (AQPELYLLNTMDADSLVSR), CI-MPR$_{2347–2375}$, and palmitoylated CI-MPR$_{2347–2375}$ with N-terminal di-lysine (KKSNVSYKYSKVNKEEETDENETEWLMEEIQ) were synthesized by GenScript (USA).

Molecular biology and cloning

pmCherry-SNX1 was generated by subcloning the full-length open reading frame of human SNX1 from pEGFP-SNX1 described previously (*94*), into the multiple cloning site of pmCherry-C1. pmCherry-Vps35 was generated by subcloning the full-length open reading frame of human Vps35 from pEGFP-Vps35 described previously (*10*), into the multiple cloning site of pmCherry-N1.

For bacterial expression, retromer constructs encoding full-length human and zebrafish Vps29, Vps26A, and Vps35 were cloned into either pET28a and pGEX4T-2 vectors as described previously (*60*, *95*). *C. thermophilum* Vps29, Vps26, and Vps35 were also cloned using a protocol described previously (*58*). In all cases, Vps26A was cloned as an N-terminal His$_6$-tag fusion protein, and Vps29 was cloned into a pGEX4T-2 vector as a cleavable N-terminal GST fusion protein. For mouse Vps26B, full-length complementary DNA (cDNA) was inserted into pMW172Kan vector (*77*). For the truncation constructs, the DNA sequence encoding the N-terminal part of Vps35 (Vps35$_{1–172}$, Vps35$_{1–224}$, and Vps35$_{1–390}$) was cloned into pGEX4T-2 vector. The Vps26 ΔC-term. tail (ΔC) constructs (Vps26A$_{9–298}$ and Vps26B$_{7–296}$) were cloned into pET28a vector containing His$_6$-tag. Full-length Vps26A phosphomimetic (pm) mutant (substituted S315E, S318E, and S321E), Vps26A$_{QRFE\text{-}AAAA}$ (substituted residues 311 to 314 to alanine), and Vps26B pm mutant (S302E, S304E, S311E, S319E, T325E, S327E, and S330E substitution) were synthetic genes by GenScript (USA). cDNA encoding full-length human SNX3 was cloned into pGEX4T-2 vector. Similarly, the cDNA encoding the human Fam21 LFa motif repeats 19 to 21 was cloned into pGEX4T-2 vector. The TBC domain of human TBC1D5 was cloned into the pMCSG9 vector containing an N-terminal GST and a tobacco etch virus (TEV) protease cleavage site. Full-length mouse SNX27 was cloned into the pMCSG7 vector containing an N-terminal His and a TEV cleavage site (*96*). The PDZ domain of mouse SNX27 was cloned into the pGEX4T2 vector similar to the one described previously (*97*). cDNA encoding *L. pneumophila* effector RidL residues 1 to 236 was also cloned into the pGEX4T2 vector. Full-length human Rab7a was cloned into pET28a vector. Site-directed mutagenesis was performed to generate mutant constructs with custom-designed primers. All constructs were verified using DNA sequencing.

RaPID screening

For the first round of RaPID selection, an mRNA library was generated by T7 polymerase–mediated in vitro transcription of a PCR-assembled DNA template, purified by polyacrylamide gel electrophoresis (PAGE), and covalently ligated to a puromycin-linked oligonucleotide with T4 RNA ligase. Puro-linked mRNA library (1.2 μM) was translated in a 150-μl in vitro translation reaction (genetically reprogrammed to incorporate L- or D-ClAC-Tyr in place of the initiator formylmethionine) at 37°C for 30 min. Peptide-mRNA fusion molecules were released from the ribosome by treatment with 17 mM EDTA for 30 min at 37°C, reverse-transcribed using moloney murine leukemia virus (M-MLV) reverse transcriptase (H−) (Promega) at 42°C for 1 hour, and buffer-exchanged to Tris-buffered saline with Tween 20 (TBS-T) using Sephadex G-25. The resulting cyclic peptide–mRNA:cDNA

library was counter-selected three times against His Pull-Down Dynabeads (Thermo Fisher Scientific) and affinity-selected against 200 nM bead-immobilized retromer for 30 min at 4°C, with the beads washed three times with TBS-T, overlaid with 0.1% Triton X-100, and heated to 95°C to elute the cDNA for recovery by PCR.

For the second and subsequent rounds of selection, the translation reaction was scaled down to 2.5 μl of total volume, and six iterative counter-selections using uncoated beads were conducted before affinity selection against retromer. Following five iterative rounds of selection, retromer ligands were identified by sequencing the final enriched cDNA using a MiSeq sequencer (Illumina).

Synthesis of cyclic peptides

Untagged peptides were synthesized at 25 μM scale on NovaPEG Rink Amide resin (0.53 mmol/g) using Fmoc-based chemistry on a Syro I peptide synthesizer (Biotage). Fmoc-protected amino acid (6 equivalents, eq.), 2-(1*H*-benzotriazol-1-yl)-1,1,3,3-tetramethyluronium hexafluorophosphate (6 eq.), hydroxybenzotriazole (6 eq.), and diisopropylethylamine (DIPEA; 12 eq.) with 30 min of coupling cycles. Deprotection of fmoc was achieved with 40% piperidine/*N*,*N*′-dimethylformamide (DMF) for 1 × 3 min and then 1 × 12 min. Chloroacetic acid was coupled manually after the final deprotection using the same conditions.

Linear peptides were cleaved from resin with trifluoroacetic acid (TFA)/triisopropylsilane (TIS)/H_2O/ethanedithiol (EDT) (92.5:2.5:2.5:2.5) for more than 2 hours. Crude peptides were precipitated and washed (five times with cold Et_2O), redissolved in dimethyl sulfoxide (DMSO), and cyclized by adding DIPEA until basic, followed by incubating at room temperature. Cyclic peptides were acidified, diluted to 50% DMSO with water, and purified by reversed-phase high-performance liquid chromatography (RP-HPLC) using a Chromolith C18 column with a gradient of 10 to 70% buffer B (99.9% CH_3CN/0.1% TFA in buffer A and 0.1% TFA in water) over 40 min and lyophilized, before the TFA salt was exchanged to HCl by triplicate lyophilization from 5 mM aqueous HCl.

Synthesis of biotinylated and FITC-labeled cyclic peptides

Biotin- and FITC-labeled peptides were synthesized (100 μM scale) on Rink Amide 4-methylbenzhydrylamine (MBHA) resin (0.6 mmol/g) using Fmoc-based chemistry and a peptide synthesizer (Symphony, Protein Technologies) Fmoc-Lys(Mtt)-OH in position 1. Fmoc-protected amino acid (4 eq.), 2-(6-chloro-1*H*-benzotriazole-1-yl)-1,1,3,3 tetramethylaminium hexafluorophosphate (4 eq.), and DIPEA (4 eq.) were used in 2 × 30 min coupling cycles. Fmoc deprotection was achieved by treatment with 1:2 piperidine/DMF for 2 × 3 min. Chloroacetic acid was coupled manually after the final deprotection using chloroacetic acid (4 eq.) and 2-(1*H*-7-azabenzotriazol-1-yl)-1,1,3,3-tetramethyl uraniumhexafluorophosphate methanaminium (HATU) (4 eq.), as well as DIPEA (4 eq.) in DMF. Selective side chain deprotection of the methyl trityl (Mtt) group on lysine was achieved using 3% TFA in dichloromethane (5 × 2 min). Biotin was coupled using biotin HATU (2 eq.) and DIPEA in DMF. FITC was coupled using FITC (2 eq.) and DIPEA.

Linear peptides were cleaved from the resin by treatment with TFA/TIS/H_2O (95:2.5:2.5) for 2 hours. The crude peptides were precipitated and washed with cold Et_2O, redissolved in 50% acetonitrile/0.05% TFA in water, and lyophilized. Peptides were purified by RP-HPLC using a Phenomenex Luna C18 column eluting at a flow rate of 20 ml/min and a gradient of 20 to 70% buffer B (90% CH_3CN/10% H_2O/0.1% TFA in buffer A and 0.1% TFA in water) over 30 min and lyophilized.

Cyclization to form the thioether was achieved by dissolving the linear peptide in DMF with DIPEA (10 eq.), and the reaction was monitored by ultra-performance liquid chromatography–mass spectrometry (UPLC-MS). After no more linear peptide was detected, DMF was removed in vacuo, and the cyclic peptide was purified by RP-HPLC using a Phenomenex Luna C18 column eluting at a flow rate of 20 ml/min and a gradient of 20 to 70% buffer B (90% CH_3CN/10% H_2O/0.1% TFA in buffer A and 0.1% TFA in water) over 30 min and lyophilized.

Peptides were characterized, and purity was determined by analytical RP-UPLC and UPLC-MS methods. UPLC was performed on Shimadzu Nexere UPLC with photodiode array (PDA) using an Agilent Eclipse plus C18 Rapid Resolution High Definition (RRHD) 1.8 μm, 2.1 × 100 mm UPLC column, and a gradient of 0 to 80% buffer B (90% CH_3CN/10% H_2O/0.1% TFA in buffer A and 0.1% TFA in water) over 6 min. UPLC-MS was performed on the Shimadzu Nexere UPLC system connected to a LCMS-2020 single quadrupole mass spectrometer using an Phenomenex Aeris Peptide 1.7 μm XB-C18 column 50 × 2.1 mm and a gradient of 0 to 80% buffer B (90% CH_3CN/10% H_2O/0.1% formic acid in buffer A and 0.1% formic acid in water) over 6 min.

Cell culture and transfection

HeLa cells (American Type Culture Collection, CCL-2) were maintained in high-glucose Dulbecco's modified Eagle's medium (DMEM; Thermo Fisher Scientific) supplemented with 10% fetal bovine serum (FBS) and 2 mM L-glutamine (Thermo Fisher Scientific) in a humidified 37°C incubator with 5% CO_2. Transfection was performed using Lipofectamine 2000 (Thermo Fisher Scientific) according to the manufacturer's instructions.

Peptide delivery by reversible permeabilization and indirect fluorescence microscopy and image analysis

Reversible permeabilization of HeLa cells with SLO (25,000 to 50,000 U; Sigma-Aldrich) was performed as previously described (*98*). Briefly, an aliquot of SLO stock was reduced by 10 mM dithiothreitol (DTT) (Sigma-Aldrich) for 20 min at 37°C and then diluted to working concentration (200×) in Dulbecco's phosphate-buffered saline (DPBS) containing 1 mM $MgCl_2$. HeLa cells grown on coverslips were incubated in the SLO-containing solution for 9 min at 37°C, washed twice with DPBS containing 1 mM $MgCl_2$, and then incubated with ice-cold transport buffer [140 mM NaCl, 5 mM KCl, 1 mM $MgCl_2$, 10 mM Hepes, and 10 mM glucose (pH 7.4)] containing fluorescent peptides (5 μg/ml) on ice for 5 min. After labeling, the cells were washed with ice-cold transport buffer twice and incubated with the recovery medium (DMEM, 10% FBS, 1.8 mM $CaCl_2$, and without antibiotics) for 20 min at 37°C. Cells were fixed with 4% paraformaldehyde (PFA) or ice-cold methanol and subjected for microscopy analysis.

HeLa cells grown on coverslips were routinely fixed and permeabilized in ice-cold methanol for 5 min at −20°C, unless otherwise cited. After blocking with 2% bovine serum albumin (BSA) in PBS for 30 min, cells were labeled with anti-TBC1D5 (1:200) and anti-SNX1 (1:100) for 1 hour at room temperature followed by the incubation with Alexa Fluor 555– and Alexa Fluor 647–conjugated secondary antibodies. Coverslips were mounted on glass microscope slides using the Fluorescence Mounting Medium (Dako), and

the images were taken at room temperature using the Leica DMi8 SP8 inverted confocal microscope equipped with 63× Plan Apochromatic objectives or the Zeiss LSM 880 Axiovert 200 inverted confocal microscope with Airyscan FAST detector equipped with 63× Plan Apochromatic objectives. For quantification, images were taken from multiple random positions for each sample.

Images were processed using ImageJ software. Colocalization analysis was performed as described previously (*99*). Briefly, single cells were segregated from fields of view by generating regions of interest (ROIs), cropped, split into separated channels, and applied for threshold processing. Colocalization analysis was conducted on three independent experiments and represented as Pearson's correlation coefficient. Colocalization values were exported to R studio and tabulated accordingly.

Peptide electroporation and indirect fluorescence microscopy and image analysis

Peptide electroporation was performed on the Neon Transfection System from Thermo Fisher Scientific according to manufacturer's instructions, adapting the protein electroporation strategy of Alex *et al.* (*72*). Briefly, aliquots of 3×10^5 HeLa cells were pelleted and resuspended in 10 μl of the electroporation buffer R (Thermo Fisher Scientific). The RT-D3 peptide or a scrambled RT-D3 control peptide were then mixed with cell suspensions to reach the final concentrations of 20 μM, while cell suspensions alone served as mock controls. The peptide/cell suspension mixtures were loaded with 10-μl Neon Pipette Tips (Thermo Fisher Scientific) and electroporated with two pulses at 1000 V for 35 ms. Electroporated cells were then transferred onto poly-L-lysine–coated glass coverslips in a 12-well plate containing the complete DMEM to allow recovery for 16 to 18 hours.

Cells grown on coverslips were fixed with 4% PFA in PBS for 15 min followed by permeabilization and blocking with 0.1% saponin in 2% BSA/PBS for 20 min. Cells were then labeled with the diluted goat polyclonal TBC1D5 antibody (1:100) and rabbit polyclonal Vps26A antibody (1:500) in 0.1% saponin followed by the corresponding fluorescently conjugated secondary antibodies for 1 hour at room temperature. Coverslips were mounted on glass microscope slides using the Fluorescence Mounting Medium (Dako), and the images were taken using a Leica DMi8 SP8 inverted confocal microscope equipped a 63× Plan Apochromatic 1.4 numerical aperture oil objective. Images were processed using Fiji/ImageJ software, and the colocalization analysis was performed using the Fiji/ImageJ EzColocalization plugin. Briefly, ~60 individual cells for each condition were randomly selected and cropped to generate and record ROIs. The selected ROI was then split into the separate channels and threshold applied before colocalization analysis by Pearson's correlation coefficient. Statistical analysis and graph generation were performed using Prism9 (GraphPad) software. Error bars on the graphs represent ±SEM. All *P* values were calculated using a Student's *t* test, and $P < 0.05$ was considered as statistically significant.

Recombinant protein expression and purification

All the retromer constructs were expressed using BL21 Star (DE3) cells and induced by the addition of isopropyl-β-D-thiogalactopyranoside (IPTG) to a final concentration of 1 mM at an OD_{600} (optical density at 600 nm) of ~0.8. The temperature was then reduced to 18°C and incubated overnight. To obtain the retromer trimer complex (including human, zebrafish and *C. thermophilum*), full-length GST-tagged Vps29 coexpressed with Vps35 was mixed with the cell pellet of Vps26A and lysed through a Constant System TS-Series cell disruptor in lysis buffer containing 50 mM Hepes (pH 7.5), 200 mM NaCl, 5% glycerol, benzamidine (50 μg/ml), and deoxyribonuclease I (DNase I). The homogenate was cleared by centrifugation and loaded onto Talon resin (Clonetech) for purification. To obtain the correct stoichiometry ratio of the retromer complex, the purified elution from the Talon resin was further passed through the glutathione Sepharose (GE Healthcare). Removal of the GST-tag from human and zebrafish Vps29 was performed using on-column cleavage with thrombin (Sigma-Aldrich) overnight at 4°C. For *C. thermophilum* Vps29, the GST-tag was cleaved using PreScission protease overnight at 4°C. The flow-through containing the retromer complex with GST-tag removed was further purified using size exclusion chromatography (SEC) on a Superdex 200 column equilibrated with a buffer containing 50 mM Hepes (pH 7.5), 200 mM NaCl, 5% glycerol, and 0.5 mM tris (2-carboxyethyl) phosphine (TCEP). Production of retromer individual subunits (Vps29, Vps26A, and Vps35) and subcomplexes (Vps29-Vps35, Vps26A-$Vps35_{1–172}$, Vps26A-$Vps35_{1–224}$, Vps26A-$Vps35_{1–390}$, $Vps26A_{\Delta C\text{-term. tail}}$-$Vps35_{1–390}$, $Vps26A_{pm}$-$Vps35_{1–390}$, $Vps26A_{QRFE\text{-}AAAA}$-$Vps35_{1–390}$, Vps26B-$Vps35_{1–390}$, $Vps26B_{\Delta C\text{-term. tail}}$-$Vps35_{1–390}$, and $Vps26B_{pm}$-$Vps35_{1–390}$) were expressed and purified under the same method. Briefly, glutathione Sepharose was used for Vps29, Vps35, and subcomplexes purification, and Talon resin was applied for Vps26A.

Expression and purification of GST-SNX3, GST-$Fam21_{R19–R21}$, GST-$TBC1D5_{TBC}$, GST-$SNX27_{PDZ}$, His-SNX27, GST-$RidL_{1–236}$, and His-Rab7a were performed using similar methods as described previously (*56*, *59*, *96*, *97*). Cell pellets were lysed with a Constant System TS-Series cell disruptor using the same buffer as retromer. All proteins were passed through either Talon resin or glutathione Sepharose depending on the affinity tag. Removal of fusion tag was performed on column overnight using either thrombin for SNX3 and $RidL_{1–236}$ or TEV protease for $SNX27_{PDZ}$ and $TBC1D5_{TBC}$. The flow-through samples containing GST-tag removed SNX3, $RidL_{1–236}$, $TBC1D5_{TBC}$, and $SNX27_{PDZ}$ were further purified using SEC in the same way as Retromer. For His-tagged SNX27 and His-Rab7a, the fractions eluted from Talon resin was further purified by SEC directly using the same buffer as described above. Similarly, the GST-tagged $Fam21_{R19–R21}$ eluted from glutathione Sepharose was directly injected into SEC for final purification.

Retromer 3KE construct design, expression, and purification has previously been described (*61*). Briefly, retromer plasmids were cotransformed into BL21(DE3) Rosetta2 pLysS cells (Millipore). Cells were grown to OD_{600} between 0.8 and 1.0 and induced for 16 to 20 hours at 20°C with 0.4 mM IPTG. Cells were lysed using a disruptor (Constant Systems Limited). Protein was purified in 10 mM tris-HCl (pH 8.0), 200 mM NaCl, and 2 mM βME using glutathione Sepharose (GE Healthcare). Protein was cleaved overnight using thrombin (Recothrom, The Medicines Company) at room temperature and batch-eluted in buffer. Retromer was further purified by gel filtration on a Superdex S200 10/300 column (GE Healthcare) into 10 mM tris-HCl (pH 8.0) and 200 mM NaCl.

Biotinylated cyclic peptide pull-down assay

Culture dishes (15 cm) with HeLa cells at approximately 90% confluency were washed with PBS and lysed by the lysis buffer containing 50 mM Hepes (pH 7.5), 200 mM NaCl, 1% Triton X-100, DNase I (25 μg/ml), and one protease inhibitor cocktail tablet per 50 ml of

lysis buffer. Soluble and insoluble fractions were separated by centrifugation at 13,000*g* for 20 min at 4°C. After centrifugation, supernatant was then added to the streptavidin agarose (Thermo Fisher Scientific) preincubated with 140 μM of either biotinylated RT-D3 or biotinylated RT-L4 cyclic peptides for 2 hours at 4°C. Both cyclic peptides were carefully prepared without forming precipitation before mixing with streptavidin agarose.

In the case of capturing SNX3, roughly 5 μM of DMT1-II$_{550–568}$ peptide was added to the supernatant before mixing with the streptavidin agarose. Beads were then spun down at 2000*g* for 2 min and washed five times with washing buffer containing 50 mM Hepes (pH 7.5), 200 mM NaCl, 5% glycerol, 0.05% Triton X-100, and 0.5 mM TCEP. Bound complex was eluted from the streptavidin agarose by boiling in 100 mM DTT-added SDS loading buffer (Life Science) and subjected to SDS-PAGE analysis and Western blotting.

RT-L4 binding site screening assay

Mapping the potential binding region of RT-L4 was carried out using purified Vps26A, Vps35$_{1–390}$, Vps26-Vps35$_{1–390}$ subcomplex, and the associated mutants. First, 10 μM purified proteins was incubated with fresh streptavidin agarose containing either 100 μM RT-L4 or equivalent percentage (v/v) of DMSO. The mixture was incubated in binding buffer containing 50 mM Hepes (pH 7.5), 200 mM NaCl, 5% glycerol, and 0.5 mM TCEP for 30 min at 4°C. Beads were then washed three times with binding buffers followed by SDS-PAGE analysis.

GST pull-down assay

GST pull-down assay was carried out using either GST-tagged retromer, GST-Fam21$_{R19\text{-}R21}$, or GST-TBC1D5$_{TBC}$ as bait protein. For pull-down assays containing either SNX27 or SNX3 + DMT1-II$_{550–548}$ peptide, GST-tagged retromer and GST alone were first incubated with fresh glutathione Sepharose bead for 2 hours at 4°C. To avoid precipitation caused by cyclic peptides, SNX3/SNX27–cyclic peptides mixture were centrifuged at 17,000 rpm for 20 min at 4°C before added into the glutathione Sepharose bead samples. The reaction mixtures were incubated for at least 4 hours in binding buffer containing 50 mM Hepes (pH 7.5), 200 mM NaCl, 5% glycerol, 0.1% Triton X-100, and 0.5 mM TCEP. Beads were then washed four times with binding buffers, and samples of beads were analyzed by SDS-PAGE. Retromer-TBC1D5 and retromer-Fam21 pull-down assays were performed using identical protocol as described above. For retromer-TBC1D5 pull-down assay, GST-TBC1D5$_{TBC}$ was used to differentiate GST-Vps29 and TBC1D5$_{TBC}$ on the SDS-PAGE.

Crystallization and data collection

Crystallization screening was performed using a hanging-drop vapor diffusion method under a 96-well format at 20°C. To cocrystallize Vps29 with cyclic peptides, 1.5-fold molar excess of the RT-D1, RT-D2, RT-D3, RT-L1, and RT-L2 peptides were added separately to the purified hVps29 to a final concentration of 14 mg/ml. Initial crystals were obtained in hVps29–RT-D1, hVps29–RT-D2, and hVps29–RT-L2 complex samples. For hVps29–RT-D1, plate shape crystals were observed in many different commercial screen conditions, but the best quality crystals were obtained in a condition comprising 3.5 M sodium formate. For hVps29–RT-D2, the optimized crystals were obtained by streak-seeding crystals grown in 0.1 M potassium thiocyanate, 30% polyethylene glycol monomethyl ether 2000 (PEG 2000 MME) into the same condition prepared with protein at 8 mg/ml. For hVps29–RT-L2 sample, precipitation was observed after the addition of the cyclic peptide. Precipitation was removed by centrifugation, and diamond-shaped crystals were obtained after overnight incubation in condition consisted of 0.1 M Hepes (pH 7.0), 1 M succinic, and 1% PEG-2000 MME. Initial attempts to cocrystallize hVps29–RT-D3 and hVps29–RT-L1 were unsuccessful. For hVps29–RT-L1, small long needle–shaped crystals were observed in condition consisted of 1.4 M sodium malonate (pH 6.0) using protein (26 mg/ml) with 1.5-fold molar excess of RT-L1 and 10-fold molar excess of 18-crown-6. Diffraction quality crystals were obtained by streak-seeding crystals grown in 26 mg/ml into the same condition prepared with protein at 15.5 mg/ml. To grow crystals containing RT-D3, we substituted hVps29 to ctVps29 and managed to obtain diffraction-quality crystals in condition consisted of 0.18 M ammonium citrate dibasic and 20% PEG-3350 using protein (14 mg/ml) with twofold molar excess RT-D3. Before data collection, all the crystals were soaked in the appropriate cryoprotectant solutions. X-ray diffraction data were measured on the MX1 and MX2 beamlines at the Australian Synchrotron at 100 K.

Crystal structure determination

All the data collected were indexed and integrated by AutoXDS (*100*) and scaled using Aimless (*101*). Crystal structures of hVps29–RT-D1, hVps29–RT-D2, ctVps29–RT-D3, hVps29–RT-L1, and hVps29–RT-L2 were solved by molecular replacement using Phaser (*102*) with native hVps29 crystal structure [Protein Data Bank (PDB) ID: 1W24] as the initial model. The initial electron density map obtained from the best solution guided the locations of the cyclic peptides and 18-crown-6. Structure refinement was performed using the PHENIX suite (*103*) with iterative rebuilding of the model. The refined model was manually rebuilded using Coot guided by $F_o - F_c$ difference maps. Coordinates for D-tyrosine and sulfanylacetic acid linking N terminus and C terminus of the peptides were generated using LIBCHECK from Coot. The quality and geometry of the refined structures were evaluated using MolProbity (*104*). Data collection and refinement statistics are summarized in table S3. Sequence conservation was based on a T-Coffee multiple sequence alignment (*105*) and calculated using the ConSurf Server (*106*). Structure comparison was analyzed using DALI (*107*), and molecular figures were generated using PyMOL.

Surface plasmon resonance

SPR experiments were conducted at room temperature using a Biacore T200 instrument (Cytiva) in HBS-P+ buffer [10 mM Hepes, 150 mM NaCl, and 0.05% (v/v) surfactant P20 (pH 7.4)] containing 0.1% (v/v) DMSO. Human or zebrafish retromer (100 nM) was immobilized on a Ni^{2+}-primed Series S Sensor Chip nitrilotriacetic acid (NTA) (Cytiva) following the manufacturer's instructions. A single-cycle kinetics protocol involving five 120-s injections of peptide as analyte at a flow rate of 60 μl min^{-1} was used, with kinetics determined using a 1:1 binding model.

Isothermal titration calorimetry

ITC experiments were conducted at 25°C using a MicroCal PEAQ-ITC (Malvern) in buffer containing 50 mM Hepes (pH 7.4), 200 mM NaCl, 5% glycerol, and 0.5 mM TCEP. Cyclic peptides in the range of 120 to 300 μM were titrated into 6 to 20 μM retromer, subcomplexes, or individual subunits. The interaction of retromer and TBC1D5$_{TBC}$ in the presence of cyclic peptide was carried out by titrating 80 μM TBC1D5$_{TBC}$ into 6 μM retromer + 30 μM of either

RT-D3 or RT-L4. In the native control, the cyclic peptide was substituted with equivalent percentage (v/v) of DMSO. Under the same experimental condition, 180 μM $RidL_{1–236}$ was titrated into 9 μM retromer with 72 μM RT-D3 or equivalent percentage (v/v) of DMSO. Similarly, the effect of the cyclic peptides on the interaction of retromer and $SNX27_{PDZ}$ was performed by titrating 1.3 mM $SNX27_{PDZ}$ into 30 μM retromer + 150 μM of either RT-D3 or RT-L4. The interaction of retromer and Fam21 was performed by titrating 300 μM GST-$Fam21_{R19–R21}$ into 12 μM retromer + 60 μM of either RT-D3 or RT-L4. In the case of SNX3, 1.2 mM SNX3 was titrated into 12 μM retromer + 180 μM DMT1-$II_{550–568}$ peptide + 60 μM of either RT-D3 or RT-L4. Similarly, 1.2 mM SNX3 was titrated into 12 μM retromer + 180 μM CI-$MPR_{2347–2376}$ peptide to examine its effect on retromer and SNX3 interaction. To ensure that RT-L4 binds specifically only to retromer but not the accessory proteins, 90 μM RT-L4 was titrated into 7 μM retromer, $TBC1D5_{TBC}$, SNX3, or SNX27 using the buffer described above. The effect of Vps26 C-terminal disordered tail on RT-L4 and SNX3 binding was first performed by titrating 90 μM RT-L4 into 8 μM Vps26A/B-$Vps35_{1–390}$ or Vps26A/$B_{\Delta C\text{-term. tail}}$-$Vps35_{1–390}$ subcomplexes. In the case of SNX3 binding, 970 μM SNX3 was titrated into 17 μM full-length (FL), pm mutant, QRFE-AAAA, or ΔC Vps26A/B-$Vps35_{1–390}$ subcomplexes with and without 255 μM DMT1-$II_{550–568}$ peptide. For the retromer, R55, and compound 2a interactions, 120 to 540 μM freshly prepared R55 or compound 2a was titrated into 9 to 16 μM retromer using the same buffer as the cyclic peptide ITC experiments.

In all cases, the experiments were performed with an initial 0.4 μl (not used in data processing) followed by 12 serial injections of 3.22 μl each with 180-s intervals. Data were analyzed with Malvern software package by fitting and normalized data to a single-site binding model, yielding the thermodynamic parameters K_d, ΔH, ΔG, and $-T\Delta S$ for all binding experiments. The stoichiometry was refined initially, and if the value was close to 1, then N was set to exactly 1.0 for calculation. All experiments were performed at least in triplicate to check for reproducibility of the data.

Differential scanning fluorimetry

Thermal unfolding experiments were carried out through preferential binding of a fluorophore to unfolded protein using a ViiA7 real-time PCR instrument (Applied Biosystems). Briefly, 0.4 mg/ml of freshly purified retromer, subcomplex, and individual subunits was preincubated with 20 to 60 molar excess of cyclic peptides, R55, or compound 2a for at least 30 min on ice followed by centrifugation at 17,000 rpm for 20 min at 4°C to remove all possible precipitation. To measure thermal denaturation, freshly prepared SYPRO orange dye (Life Science) was then added to protein–cyclic peptide complex mixture to a final concentration of five times before loaded into the 96-well plate. Relative fluorescence units were measured from 25° to 90°C using the ROX dye calibration setting at 1°C increments. Experiments were performed with four replicates, and T_m was calculated using Boltzmann sigmoidal in Prism version 8.0.1 (GraphPad Software).

Mass photometry

Molecular mass measurement of retromer in the presence of cyclic peptide was performed using a Refeyn OneMP mass photometer (Refeyn Ltd). Briefly, 10 μl of standard buffer containing 50 mM Hepes (pH 7.5) and 200 mM NaCl was applied. Next, 1 μl of 50 nM retromer + RT-D3 and RT-L4 cyclic peptide was added to the drop to a final concentration of 5 nM, and 10,000 frames were recorded. Calibration was performed using three protein standards (i.e., 66, 146, and 480 kDa) (Thermo Fisher Scientific).

GTPase activity assay

The Rab7 GAP activity of TBC1D5 in the presence of retromer and cyclic peptides was carried out using the GTPase-Glo assay kit (Promega) according to the manufacturer's instructions. Briefly, 10 μM Rab7a containing 10 μM GTP and 1 mM DTT in GTPase/GAP buffer was incubated with 3 μM $TBC1D5_{TBC}$, 6 μM retromer, and 60 μM cyclic peptides or equivalent percentage (v/v) of DMSO for 60 min at room temperature. For the Rab7a-only experiment, 10 μM Rab7a was incubated with 60 μM cyclic peptides without $TBC1D5_{TBC}$ or retromer. Similarly, $TBC1D5_{TBC}$-only experiments were performed by incubating 10 μM Rab7a with 3 μM $TBC1D5_{TBC}$ and 60 μM cyclic peptides without retromer. Opposite reactions were also prepared for retromer only experiments. To complete the GTPase reaction, an equal volume of the reconstituted GTPase-Glo reagent containing 5 μM adenosine diphosphate was then added to the reaction mix and incubated for a further 30 min at room temperature. The luminescence of residual GTP after GTPase reaction was measured by adding detection reagent to the reaction mix and recorded using an Infinite M1000 PRO multimode microplate reader (Tecan) at 25°C.

Cryo-EM grid preparation and data collection

For cryo-EM of retromer + RT-L4, retromer 3KE at a final concentration of 0.5 mM in 20 mM tris (pH 8.0)/100 mM NaCl/2 mM DTT was combined with RT-L4 at a final concentration of 0.1 mM, incubated for 1 hour, and spun briefly in a tabletop centrifuge. Two microliters of the sample was applied to freshly glow-discharged Quantifoil 1.2/1.3 300 mesh grids, and the grids were vitrified in liquid ethane using a Thermo Fisher Scientific Mark IV Vitrobot, using a 3.5-s blot time at 100% humidity and 20°C. Four thousand seven hundred ninety-one micrographs were collected on a Thermo Fisher Scientific FEI Titan Krios G3i microscope in the Center for Structural Biology's Cryo-EM Facility at Vanderbilt. The microscope was operated at 300 keV and was equipped with a Thermo Fisher Scientific Falcon 3 direct electron detector camera. The nominal magnification used during data collection was ×120,000, and the pixel size was 0.6811 Å per pixel. The total electron dose was 50 e^-/A^2, and micrographs were collected at ±30° tilts. Data collection was accomplished using EPU (Thermo Fisher Scientific).

For cryo-EM of apo retromer, 2 μl of wild-type retromer at a concentration of 0.5 mM in 20 mM tris (pH 8.0)/100 mM NaCl/2 mM DTT was applied to freshly glow-discharged QUANTIFOIL 1.2/1.3 300 mesh grids, and the grids were vitrified in liquid ethane using a Thermo Fisher Scientific Mark IV Vitrobot, using a 2-s blot time at 100% humidity and 8°C. Eight hundred ninety-one micrographs were collected on a Thermo Fisher Scientific FEI Titan Krios microscope at the National Resource for Automated Molecular Microscopy (NRAMM). The microscope was operated at 300 keV and was equipped with a Gatan BioQuantum energy filter with a slit width of 20 eV and a Gatan K2 Summit direct electron detector camera. The nominal magnification used during data collection was ×105,000, and the pixel size was 1.0691 Å per pixel. The total electron dose was 73.92 e^-/A^2, and micrographs were collected at ±15° tilts. Data collection was accomplished using Leginon (*108*).

Single-particle cryo-EM image and data processing

All images were motion-corrected using MotionCor2 (*109*). Micrographs from the apo retromer data collection were rescaled to

match the pixel size (1.096 Å per pixel) from published data collections (*61*) using an NRAMM script written for MotionCor2. The contrast transfer function (CTF) of each micrograph was determined using Gctf (*110*). Defocus values for the retromer/RT-L4 data varied between −0.8 and −2.6 μm; defocus values for the apo retromer data varied between −0.8 and −4.7 μm. RELION-3 (*111*) was used for all image processing unless otherwise indicated.

Retromer/RT-L4 processing

Micrographs were autopicked using a 20-Å low-pass–filtered three-dimensional (3D) model that had been produced in early rounds of processing, and this template-based autopicking identified 968,806 particles. Multiple rounds of 2D classification yielded 171,270 particles suitable to continue to 3D classification. The same 3D model used for autopicking was filtered to 60 Å and used as an initial model for 3D classification. The particles underwent multiple rounds of CTF refinement and Bayesian polishing to produce a final set of 28,083 particles suitable for 3D refinement and postprocessing. The final masked model had a resolution of 5.9 Å and a RELION-determined B factor of −88.

Apo Retromer processing

Data giving rise to the published apo retromer reconstruction lacked tilted views (table S5); an additional dataset (table S5, data collection #3) was collected to add tilted views and to improve the reconstruction for this study. Several thousand particles were manually selected from dataset #3 (table S5) to perform initial 2D classification and produce templates for autopicking. Template-based autopicking identified 207,026 particles, which were subjected to initial 2D and 3D classification and refinement as well as CTF refinement. Particles (250,500) from data collection #1 and #2 (table S5) retromer datasets (*61*) were imported to combine with data collection #3. Multiple rounds of 2D classification yielded 72,795 particles suitable to continue to 3D classification. Initial models for 3D classification (*61*) were filtered to 60-Å resolution for use in these experiments. The particles underwent multiple rounds of CTF refinement and Bayesian polishing to produce a final set of 43,808 particles suitable for 3D refinement and postprocessing. The final masked model had a resolution of 4.9 Å and a RELION-determined B factor of −113.799.

For both reconstructions, rigid-body docking and map visualization were performed in Chimera (*112*) using the Fit in Map routine. Models for N-VPS35 and VPS26A subunits were obtained from PDB 5F0J.

Liposome preparation

Sucrose-loaded liposome binding assay were performed using the standard extrusion method with some modification (*113*). Briefly, cargo-loaded Folch liposomes were made by mixing 25 μl of N-terminal palmitoylated CI-MPR$_{2347–2376}$ peptide (4 mg/ml), 50 μl of Folch fraction I (Sigma-Aldrich) (10 mg/ml), and 50 μl of di-C16 PtdIns(3)*P* (1 mg/ml) (Echelon Biosciences), each freshly prepared in chloroform, to a total volume of 500 μl of chloroform. The solution was dried down on the walls of a mini round-bottom flask under a N_2 stream and left overnight in a vacuum desiccator to yield a lipid film. This yields liposomes with a final PtdIns(3)*P* ratio of 10% (w/v). For PC/PE liposome, 50 μl of stock (10 mg/ml) of 1-palmitoyl-2-oleoyl-*sn*-glycero-3-phosphocholine (POPC) and 1-palmitoyl-2-oleoyl phosphatidylethanolamine (POPE) in a 9:1 ratio (Avanti Polar Lipids) was freshly prepared in a 500-μl volume, and lipid films formed using the same method as Folch liposomes. This results in a POPC/POPE liposome in a 90:10% (w/v) ratio. To form multilamellar vesicles (MLVs), the lipid films were hydrated with a buffer comprising 20 mM Hepes (pH 7.5) and 220 mM sucrose with agitation, followed by 10 cycles of rapid freeze-thaw. The sucrose-loaded heavy MLVs were centrifuged at 180,000*g* for 30 min at 4°C using an Optima TL benchtop ultracentrifuge (Beckman Coulter). The resulting pellets were buffer-exchanged by resuspension into the assay buffer comprising 50 mM Hepes (pH 7.5), 125 mM NaCl, and 0.5 mM TCEP. To avoid buffer mismatch, the protein samples were also buffer-exchanged into the same buffer.

Liposome binding assays

The binding assay was performed in a total volume of 80 μl comprising 40 μl of sucrose-loaded MLVs and 7 μM retromer, 7 μM SNX3, or 7 μM retromer-SNX3 mixture in a 1-to-1 ratio. The reaction mixtures were incubated at room temperature for 15 min followed by centrifugation at 36,000*g* using an Optima TL benchtop ultracentrifuge (Beckman Coulter) for 15 min at 4°C. The supernatant and pelleted fractions were then carefully separated. The pellet was then resuspended in 80 μl of buffer containing 50 mM Hepes (pH 7.5), 125 mM NaCl, and 0.5 mM TCEP before analyzed by SDS-PAGE.

Statistics

Statistical analysis was completed in R studio using dplyr, ggplot2, and ggpubr packages. Error bars on graphs were represented as the SEM (±SEM). *P* values were calculated using the two-tailed Student's *t* test. $P < 0.05$ was considered as significant.

SUPPLEMENTARY MATERIALS

Supplementary material for this article is available at https://science.org/doi/10.1126/sciadv.abg4007

View/request a protocol for this paper from *Bio-protocol*.

REFERENCES AND NOTES

1. P. J. Cullen, F. Steinberg, To degrade or not to degrade: Mechanisms and significance of endocytic recycling. *Nat. Rev. Mol. Cell Biol.* **19**, 679–696 (2018).
2. K. E. Chen, M. D. Healy, B. M. Collins, Towards a molecular understanding of endosomal trafficking by Retromer and Retriever. *Traffic* **20**, 465–478 (2019).
3. S. Weeratunga, B. Paul, B. M. Collins, Recognising the signals for endosomal trafficking. *Curr. Opin. Cell Biol.* **65**, 17–27 (2020).
4. C. Burd, P. J. Cullen, Retromer: A master conductor of endosome sorting. *Cold Spring Harb. Perspect. Biol.* **6**, a016774 (2014).
5. N. Heucken, R. Ivanov, The retromer, sorting nexins and the plant endomembrane protein trafficking. *J. Cell Sci.* **131**, jcs203695 (2018).
6. M. Ma, C. G. Burd, Retrograde trafficking and plasma membrane recycling pathways of the budding yeast Saccharomyces cerevisiae. *Traffic* **21**, 45–59 (2020).
7. M. N. J. Seaman, Retromer and its role in regulating signaling at endosomes. *Prog. Mol. Subcell. Biol.* **57**, 137–149 (2018).
8. M. N. Seaman, J. M. McCaffery, S. D. Emr, A membrane coat complex essential for endosome-to-Golgi retrograde transport in yeast. *J. Cell Biol.* **142**, 665–681 (1998).
9. H. Zhang, T. Huang, Y. Hong, W. Yang, X. Zhang, H. Luo, H. Xu, X. Wang, The retromer complex and sorting nexins in neurodegenerative diseases. *Front. Aging Neurosci.* **10**, 79 (2018).
10. J. Follett, S. J. Norwood, N. A. Hamilton, M. Mohan, O. Kovtun, S. Tay, Y. Zhe, S. A. Wood, G. D. Mellick, P. A. Silburn, B. M. Collins, A. Bugarcic, R. D. Teasdale, The Vps35 D620N mutation linked to Parkinson's disease disrupts the cargo sorting function of retromer. *Traffic* **15**, 230–244 (2014).
11. S. A. Small, G. A. Petsko, Retromer in Alzheimer disease, Parkinson disease and other neurological disorders. *Nat. Rev. Neurosci.* **16**, 126–132 (2015).
12. C. Vilariño-Güell, C. Wider, O. A. Ross, J. C. Dachsel, J. M. Kachergus, S. J. Lincoln, A. I. Soto-Ortolaza, S. A. Cobb, G. J. Wilhoite, J. A. Bacon, B. Behrouz, H. L. Melrose, E. Hentati, A. Puschmann, D. M. Evans, E. Conibear, W. W. Wasserman, J. O. Aasly, P. R. Burkhard, R. Djaldetti, J. Ghika, F. Hentati, A. Krygowska-Wajs, T. Lynch, E. Melamed,

A. Rajput, A. H. Rajput, A. Solida, R.-M. Wu, R. J. Uitti, Z. K. Wszolek, F. Vingerhoets, M. J. Farrer, VPS35 mutations in Parkinson disease. *Am. J. Hum. Genet.* **89**, 162–167 (2011).
13. E. T. Williams, X. Chen, D. J. Moore, VPS35, the Retromer Complex and Parkinson's Disease. *J. Parkinsons Dis.* **7**, 219–233 (2017).
14. E. Zavodszky, M. N. J. Seaman, K. Moreau, M. Jimenez-Sanchez, S. Y. Breusegem, M. E. Harbour, D. C. Rubinsztein, Mutation in VPS35 associated with Parkinson's disease impairs WASH complex association and inhibits autophagy. *Nat. Commun.* **5**, 3828 (2014).
15. A. Zimprich, A. Benet-Pagès, W. Struhal, E. Graf, S. H. Eck, M. N. Offman, D. Haubenberger, S. Spielberger, E. C. Schulte, P. Lichtner, S. C. Rossle, N. Klopp, E. Wolf, K. Seppi, W. Pirker, S. Presslauer, B. Mollenhauer, R. Katzenschlager, T. Foki, C. Hotzy, E. Reinthaler, A. Harutyunyan, R. Kralovics, A. Peters, F. Zimprich, T. Brücke, W. Poewe, E. Auff, C. Trenkwalder, B. Rost, G. Ransmayr, J. Winkelmann, T. Meitinger, T. M. Strom, A mutation in VPS35, encoding a subunit of the retromer complex, causes late-onset Parkinson disease. *Am. J. Hum. Genet.* **89**, 168–175 (2011).
16. S. A. Small, K. Kent, A. Pierce, C. Leung, M. S. Kang, H. Okada, L. Honig, J. P. Vonsattel, T. W. Kim, Model-guided microarray implicates the retromer complex in Alzheimer's disease. *Ann. Neurol.* **58**, 909–919 (2005).
17. P. Tammineni, Y. Y. Jeong, T. Feng, D. Aikal, Q. Cai, Impaired axonal retrograde trafficking of the retromer complex augments lysosomal deficits in Alzheimer's disease neurons. *Hum. Mol. Genet.* **26**, 4352–4366 (2017).
18. B. N. Vardarajan, S. Y. Bruesegem, M. E. Harbour, R. Inzelberg, R. Friedland, P. St. George-Hyslop, M. N. J. Seaman, L. A. Farrer, Identification of Alzheimer disease-associated variants in genes that regulate retromer function. *Neurobiol. Aging* **33**, 2231.e15–2231.e30 (2012).
19. L. Wen, F. L. Tang, Y. Hong, S. W. Luo, C. L. Wang, W. He, C. Shen, J. U. Jung, F. Xiong, D. H. Lee, Q. G. Zhang, D. Brann, T. W. Kim, R. Yan, L. Mei, W. C. Xiong, VPS35 haploinsufficiency increases Alzheimer's disease neuropathology. *J. Cell Biol.* **195**, 765–779 (2011).
20. L. Muzio, R. Sirtori, D. Gornati, S. Eleuteri, A. Fossaghi, D. Brancaccio, L. Manzoni, L. Ottoboni, L. D. Feo, A. Quattrini, E. Mastrangelo, L. Sorrentino, E. Scalone, G. Comi, L. Marinelli, N. Riva, M. Milani, P. Seneci, G. Martino, Retromer stabilization results in neuroprotection in a model of Amyotrophic Lateral Sclerosis. *Nat. Commun.* **11**, 3848 (2020).
21. K. J. McMillan, H. C. Korswagen, P. J. Cullen, The emerging role of retromer in neuroprotection. *Curr. Opin. Cell Biol.* **47**, 72–82 (2017).
22. I. J. McGough, F. Steinberg, D. Jia, P. A. Barbuti, K. J. McMillan, K. J. Heesom, A. L. Whone, M. A. Caldwell, D. D. Billadeau, M. K. Rosen, P. J. Cullen, Retromer binding to FAM21 and the WASH complex is perturbed by the Parkinson disease-linked VPS35(D620N) mutation. *Curr. Biol.* **24**, 1670–1676 (2014).
23. M. E. Otero-Ramirez, T. Passioura, H. Suga, Structural features and binding modes of thioether-cyclized peptide ligands. *Biomedicine* **6**, 116 (2018).
24. A. W. Fjorback, M. Seaman, C. Gustafsen, A. Mehmedbasic, S. Gokool, C. Wu, D. Militz, V. Schmidt, P. Madsen, J. R. Nyengaard, T. E. Willnow, E. I. Christensen, W. B. Mobley, A. Nykjaer, O. M. Andersen, Retromer binds the FANSHY sorting motif in SorLA to regulate amyloid precursor protein sorting and processing. *J. Neurosci.* **32**, 1467–1480 (2012).
25. K. J. McMillan, M. Gallon, A. P. Jellett, T. Clairfeuille, F. C. Tilley, I. McGough, C. M. Danson, K. J. Heesom, K. A. Wilkinson, B. M. Collins, P. J. Cullen, Atypical parkinsonism-associated retromer mutant alters endosomal sorting of specific cargo proteins. *J. Cell Biol.* **214**, 389–399 (2016).
26. L. N. Munsie, A. J. Milnerwood, P. Seibler, D. A. Beccano-Kelly, I. Tatarnikov, J. Khinda, M. Volta, C. Kadgien, L. P. Cao, L. Tapia, C. Klein, M. J. Farrer, Retromer-dependent neurotransmitter receptor trafficking to synapses is altered by the Parkinson's disease VPS35 mutation p.D620N. *Hum. Mol. Genet.* **24**, 1691–1703 (2015).
27. F. L. Tang, J. R. Erion, Y. Tian, W. Liu, D. M. Yin, J. Ye, B. Tang, L. Mei, W. C. Xiong, VPS35 in dopamine neurons is required for endosome-to-golgi retrieval of lamp2a, a receptor of chaperone-mediated autophagy that is critical for α-synuclein degradation and prevention of pathogenesis of parkinson's disease. *J. Neurosci.* **35**, 10613–10628 (2015).
28. A. Jimenez-Orgaz, A. Kvainickas, H. Nägele, J. Denner, S. Eimer, J. Dengjel, F. Steinberg, Control of RAB7 activity and localization through the retromer-TBC1D5 complex enables RAB7-dependent mitophagy. *EMBO J.* **37**, 235–254 (2018).
29. F. L. Tang, W. Liu, J. X. Hu, J. R. Erion, J. Ye, L. Mei, W. C. Xiong, VPS35 deficiency or mutation causes dopaminergic neuronal loss by impairing mitochondrial fusion and function. *Cell Rep.* **12**, 1631–1643 (2015).
30. W. Wang, X. Ma, L. Zhou, J. Liu, X. Zhu, A conserved retromer sorting motif is essential for mitochondrial DLP1 recycling by VPS35 in Parkinson's disease model. *Hum. Mol. Genet.* **26**, 781–789 (2017).
31. W. Wang, X. Wang, H. Fujioka, C. Hoppel, A. L. Whone, M. A. Caldwell, P. J. Cullen, J. Liu, X. Zhu, Parkinson's disease-associated mutant VPS35 causes mitochondrial dysfunction by recycling DLP1 complexes. *Nat. Med.* **22**, 54–63 (2016).
32. X. Chen, J. K. Kordich, E. T. Williams, N. Levine, A. Cole-Strauss, L. Marshall, V. Labrie, J. Ma, J. W. Lipton, D. J. Moore, Parkinson's disease-linkedD620N VPS35 knockin mice manifest tau neuropathology and dopaminergic neurodegeneration. *Proc. Natl. Acad. Sci. U.S.A.* **116**, 5765–5774 (2019).
33. J. Follett, A. Bugarcic, Z. Yang, N. Ariotti, S. J. Norwood, B. M. Collins, R. G. Parton, R. D. Teasdale, Parkinson disease-linked Vps35 R524W mutation impairs the endosomal association of retromer and induces α-synuclein aggregation. *J. Biol. Chem.* **291**, 18283–18298 (2016).
34. F. L. Tang, L. Zhao, Y. Zhao, D. Sun, X. J. Zhu, L. Mei, W. C. Xiong, Coupling of terminal differentiation deficit with neurodegenerative pathology in Vps35-deficient pyramidal neurons. *Cell Death Differ.* **27**, 2099–2116 (2020).
35. R. Bayliss, J. Wheeldon, S. M. Caucheteux, C. M. Niessen, V. Piguet, Identification of host trafficking genes required for HIV-1 virological synapse formation in dendritic cells. *J. Virol.* **94**, (2020).
36. E. Groppelli, A. C. Len, L. A. Granger, C. Jolly, Retromer regulates HIV-1 envelope glycoprotein trafficking and incorporation into virions. *PLOS Pathog.* **10**, e1004518 (2014).
37. J. C. Hsiao, L. W. Chu, Y. T. Lo, S. P. Lee, T. J. Chen, C. Y. Huang, Y. H. Ping, W. Chang, Intracellular transport of vaccinia virus in HeLa cells requires WASH-VPEF/FAM21-retromer complexes and recycling molecules Rab11 and Rab22. *J. Virol.* **89**, 8365–8382 (2015).
38. A. Popa, W. Zhang, M. S. Harrison, K. Goodner, T. Kazakov, E. C. Goodwin, A. Lipovsky, C. G. Burd, D. DiMaio, Direct binding of retromer to human papillomavirus type 16 minor capsid protein L2 mediates endosome exit during viral infection. *PLOS Pathog.* **11**, e1004699 (2015).
39. Z. Daniloski, T. X. Jordan, H.-H. Wessels, D. A. Hoagland, S. Kasela, M. Legut, S. Maniatis, E. P. Mimitou, L. Lu, E. Geller, O. Danziger, B. R. Rosenberg, H. Phatnani, P. Smibert, T. Lappalainen, B. R. tenOever, N. E. Sanjana, Identification of required host factors for SARS-CoV-2 infection in human cells. *Cell* **184**, 92–105.16 (2021).
40. K. Bärlocher, C. A. J. Hutter, A. L. Swart, B. Steiner, A. Welin, M. Hohl, F. Letourneur, M. A. Seeger, H. Hilbi, Structural insights into *Legionella* RidL-Vps29 retromer subunit interaction reveal displacement of the regulator TBC1D5. *Nat. Commun.* **8**, 1543 (2017).
41. I. Finsel, C. Ragaz, C. Hoffmann, C. F. Harrison, S. Weber, V. A. van Rahden, L. Johannes, H. Hilbi, The Legionella effector RidL inhibits retrograde trafficking to promote intracellular replication. *Cell Host Microbe* **14**, 38–50 (2013).
42. H. E. Miller, C. L. Larson, R. A. Heinzen, Actin polymerization in the endosomal pathway, but not on the Coxiella-containing vacuole, is essential for pathogen growth. *PLOS Pathog.* **14**, e1007005 (2018).
43. M. Romano-Moreno, A. L. Rojas, C. D. Williamson, D. C. Gershlick, M. Lucas, M. N. Isupov, J. S. Bonifacino, M. P. Machner, A. Hierro, Molecular mechanism for the subversion of the retromer coat by the Legionella effector RidL. *Proc. Natl. Acad. Sci. U.S.A.* **114**, E11151–E11160 (2017).
44. J. Yao, F. Yang, X. Sun, S. Wang, N. Gan, Q. Liu, D. Liu, X. Zhang, D. Niu, Y. Wei, C. Ma, Z. Q. Luo, Q. Sun, D. Jia, Mechanism of inhibition of retromer transport by the bacterial effector RidL. *Proc. Natl. Acad. Sci. U.S.A.* **115**, E1446–E1454 (2018).
45. P. Zhang, G. Monteiro da Silva, C. Deatherage, C. Burd, D. DiMaio, Cell-penetrating peptide mediates intracellular membrane passage of human papillomavirus L2 protein to trigger retrograde trafficking. *Cell* **174**, 1465–1476.e13 (2018).
46. B. Boland, W. H. Yu, O. Corti, B. Mollereau, A. Henriques, E. Bezard, G. M. Pastores, D. C. Rubinsztein, R. A. Nixon, M. R. Duchen, G. R. Mallucci, G. Kroemer, B. Levine, E. L. Eskelinen, F. Mochel, M. Spedding, C. Louis, O. R. Martin, M. J. Millan, Promoting the clearance of neurotoxic proteins in neurodegenerative disorders of ageing. *Nat. Rev. Drug Discov.* **17**, 660–688 (2018).
47. S. A. Small, S. Simoes-Spassov, R. Mayeux, G. A. Petsko, Endosomal traffic jams represent a pathogenic hub and therapeutic target in Alzheimer's disease. *Trends Neurosci.* **40**, 592–602 (2017).
48. V. J. Mecozzi, D. E. Berman, S. Simoes, C. Vetanovetz, M. R. Awal, V. M. Patel, R. T. Schneider, G. A. Petsko, D. Ringe, S. A. Small, Pharmacological chaperones stabilize retromer to limit APP processing. *Nat. Chem. Biol.* **10**, 443–449 (2014).
49. J. G. Li, J. Chiu, M. Ramanjulu, B. E. Blass, D. Pratico, A pharmacological chaperone improves memory by reducing Aβ and tau neuropathology in a mouse model with plaques and tangles. *Mol. Neurodegener.* **15**, 1 (2020).
50. G. Lin, P.-T. Lee, K. Chen, D. Mao, K. L. Tan, Z. Zuo, W.-W. Lin, L. Wang, H. J. Bellen, Phospholipase PLA2G6, a Parkinsonism-associated gene, affects Vps26 and Vps35, retromer function, and ceramide levels, similar to α-synuclein gain. *Cell Metab.* **28**, 605–618.e6 (2018).
51. J. E. Young, L. K. Fong, H. Frankowski, G. A. Petsko, S. A. Small, L. S. B. Goldstein, Stabilizing the retromer complex in a human stem cell model of Alzheimer's disease reduces TAU phosphorylation independently of amyloid precursor protein. *Stem Cell Rep.* **10**, 1046–1058 (2018).
52. N. K. Bashiruddin, H. Suga, Construction and screening of vast libraries of natural product-like macrocyclic peptides using in vitro display technologies. *Curr. Opin. Chem. Biol.* **24**, 131–138 (2015).

53. C. J. Hipolito, H. Suga, Ribosomal production and in vitro selection of natural product-like peptidomimetics: The FIT and RaPID systems. *Curr. Opin. Chem. Biol.* **16**, 196–203 (2012).
54. T. Passioura, H. Suga, A RaPID way to discover nonstandard macrocyclic peptide modulators of drug targets. *Chem. Commun.* **53**, 1931–1940 (2017).
55. H. Suga, Max-Bergmann award lecture: A RaPID way to discover bioactive nonstandard peptides assisted by the flexizyme and FIT systems. *J. Pept. Sci.* **24**, (2018).
56. D. Jia, J. S. Zhang, F. Li, J. Wang, Z. Deng, M. A. White, D. G. Osborne, C. Phillips-Krawczak, T. S. Gomez, H. Li, A. Singla, E. Burstein, D. D. Billadeau, M. K. Rosen, Structural and mechanistic insights into regulation of the retromer coat by TBC1d5. *Nat. Commun.* **7**, 13305 (2016).
57. A. Hierro, A. L. Rojas, R. Rojas, N. Murthy, G. Effantin, A. V. Kajava, A. C. Steven, J. S. Bonifacino, J. H. Hurley, Functional architecture of the retromer cargo-recognition complex. *Nature* **449**, 1063–1067 (2007).
58. O. Kovtun, N. Leneva, Y. S. Bykov, N. Ariotti, R. D. Teasdale, M. Schaffer, B. D. Engel, D. J. Owen, J. A. G. Briggs, B. M. Collins, Structure of the membrane-assembled retromer coat determined by cryo-electron tomography. *Nature* **561**, 561–564 (2018).
59. M. Lucas, D. C. Gershlick, A. Vidaurrazaga, A. L. Rojas, J. S. Bonifacino, A. Hierro, Structural mechanism for cargo recognition by the retromer complex. *Cell* **167**, 1623–1635.e14 (2016).
60. S. J. Norwood, D. J. Shaw, N. P. Cowieson, D. J. Owen, R. D. Teasdale, B. M. Collins, Assembly and solution structure of the core retromer protein complex. *Traffic* **12**, 56–71 (2011).
61. A. K. Kendall, B. Xie, P. Xu, J. Wang, R. Burcham, M. N. Frazier, E. Binshtein, H. Wei, T. R. Graham, T. Nakagawa, L. P. Jackson, Mammalian retromer is an adaptable scaffold for cargo sorting from endosomes. *Structure* **28**, 393–405.e4 (2020).
62. G. G. Hesketh, I. Pérez-Dorado, L. P. Jackson, L. Wartosch, I. B. Schäfer, S. R. Gray, A. J. McCoy, O. B. Zeldin, E. F. Garman, M. E. Harbour, P. R. Evans, M. N. J. Seaman, J. P. Luzio, D. J. Owen, VARP is recruited on to endosomes by direct interaction with retromer, where together they function in export to the cell surface. *Dev. Cell* **29**, 591–606 (2014).
63. H. Crawley-Snowdon, J. C. Yang, N. R. Zaccai, L. J. Davis, L. Wartosch, E. K. Herman, N. A. Bright, J. S. Swarbrick, B. M. Collins, L. P. Jackson, M. N. J. Seaman, J. P. Luzio, J. B. Dacks, D. Neuhaus, D. J. Owen, Mechanism and evolution of the Zn-fingernail required for interaction of VARP with VPS29. *Nat. Commun.* **11**, 5031 (2020).
64. D. Jia, T. S. Gomez, D. D. Billadeau, M. K. Rosen, Multiple repeat elements within the FAM21 tail link the WASH actin regulatory complex to the retromer. *Mol. Biol. Cell* **23**, 2352–2361 (2012).
65. M. Gallon, T. Clairfeuille, F. Steinberg, C. Mas, R. Ghai, R. B. Sessions, R. D. Teasdale, B. M. Collins, P. J. Cullen, A unique PDZ domain and arrestin-like fold interaction reveals mechanistic details of endocytic recycling by SNX27-retromer. *Proc. Natl. Acad. Sci. U.S.A.* **111**, E3604–E3613 (2014).
66. E. Helfer, M. E. Harbour, V. Henriot, G. Lakisic, C. Sousa-Blin, L. Volceanov, M. N. J. Seaman, A. Gautreau, Endosomal recruitment of the WASH complex: Active sequences and mutations impairing interaction with the retromer. *Biol. Cell.* **105**, 191–207 (2013).
67. M. S. Harrison, C. S. Hung, T. T. Liu, R. Christiano, T. C. Walther, C. G. Burd, A mechanism for retromer endosomal coat complex assembly with cargo. *Proc. Natl. Acad. Sci. U.S.A.* **111**, 267–272 (2014).
68. P. V. Hornbeck, B. Zhang, B. Murray, J. M. Kornhauser, V. Latham, E. Skrzypek, PhosphoSitePlus, 2014: Mutations, PTMs and recalibrations. *Nucleic Acids Res.* **43**, D512–D520 (2015).
69. A. Bugarcic, Y. Zhe, M. C. Kerr, J. Griffin, B. M. Collins, R. D. Teasdale, Vps26A and Vps26B subunits define distinct retromer complexes. *Traffic* **12**, 1759–1773 (2011).
70. K. W. Teng, Y. Ishitsuka, P. Ren, Y. Youn, X. Deng, P. Ge, S. H. Lee, A. S. Belmont, P. R. Selvin, Labeling proteins inside living cells using external fluorophores for microscopy. *eLife* **5**, e20378 (2016).
71. M. E. Harbour, S. Y. A. Breusegem, R. Antrobus, C. Freeman, E. Reid, M. N. J. Seaman, The cargo-selective retromer complex is a recruiting hub for protein complexes that regulate endosomal tubule dynamics. *J. Cell Sci.* **123**, 3703–3717 (2010).
72. A. Alex, V. Piano, S. Polley, M. Stuiver, S. Voss, G. Ciossani, K. Overlack, B. Voss, S. Wohlgemuth, A. Petrovic, Y. Wu, P. Selenko, A. Musacchio, S. Maffini, Electroporated recombinant proteins as tools for in vivo functional complementation, imaging and chemical biology. *eLife* **8**, e48287 (2019).
73. K. Patel, L. J. Walport, J. L. Walshe, P. Solomon, J. K. K. Low, D. H. Tran, K. S. Mouradian, A. P. G. Silva, L. Wilkinson-White, J. M. Matthews, J. M. Guss, R. J. Payne, T. Passioura, H. Suga, J. P. Mackay, Cyclic peptides can engage a single binding pocket through multiple, entirely divergent modes. *bioRxiv* , 850321 (2019).
74. K. E. McNally, R. Faulkner, F. Steinberg, M. Gallon, R. Ghai, D. Pim, P. Langton, N. Pearson, C. M. Danson, H. Nägele, L. L. Morris, A. Singla, B. L. Overlee, K. J. Heesom, R. Sessions, L. Banks, B. M. Collins, I. Berger, D. D. Billadeau, E. Burstein, P. J. Cullen, Retriever is a multiprotein complex for retromer-independent endosomal cargo recycling. *Nat. Cell Biol.* **19**, 1214–1225 (2017).
75. S. Banos-Mateos, A. L. Rojas, A. Hierro, VPS29, a tweak tool of endosomal recycling. *Curr. Opin. Cell Biol.* **59**, 81–87 (2019).
76. N. Leneva, O. Kovtun, D. R. Morado, J. A. G. Briggs, D. J. Owen, Architecture and mechanism of metazoan retromer:SNX3 tubular coat assembly. *Sci. Adv.* **7**, eabf8598 (2021).
77. B. M. Collins, S. J. Norwood, M. C. Kerr, D. Mahony, M. N. J. Seaman, R. D. Teasdale, D. J. Owen, Structure of Vps26B and mapping of its interaction with the retromer protein complex. *Traffic* **9**, 366–379 (2008).
78. M. C. Kerr, J. S. Bennetts, F. Simpson, E. C. Thomas, C. Flegg, P. A. Gleeson, C. Wicking, R. D. Teasdale, A novel mammalian retromer component, Vps26B. *Traffic* **6**, 991–1001 (2005).
79. F. M. Menzies, A. Fleming, A. Caricasole, C. F. Bento, S. P. Andrews, A. Ashkenazi, J. Füllgrabe, A. Jackson, M. Jimenez Sanchez, C. Karabiyik, F. Licitra, A. Lopez Ramirez, M. Pavel, C. Puri, M. Renna, T. Ricketts, L. Schlotawa, M. Vicinanza, H. Won, Y. Zhu, J. Skidmore, D. C. Rubinsztein, Autophagy and neurodegeneration: Pathogenic mechanisms and therapeutic opportunities. *Neuron* **93**, 1015–1034 (2017).
80. W. H. Toh, P. A. Gleeson, Dysregulation of intracellular trafficking and endosomal sorting in Alzheimer's disease: Controversies and unanswered questions. *Biochem. J.* **473**, 1977–1993 (2016).
81. P. Zhang, R. Moreno, P. F. Lambert, D. DiMaio, Cell-penetrating peptide inhibits retromer-mediated human papillomavirus trafficking during virus entry. *Proc. Natl. Acad. Sci. U.S.A.* **117**, 6121–6128 (2020).
82. J. Chu, D. Pratico, The retromer complex system in a transgenic mouse model of AD: Influence of age. *Neurobiol. Aging* **52**, 32–38 (2017).
83. V. Singh, J. Yang, J. Yin, R. Cole, M. Tse, D. E. Berman, S. A. Small, G. Petsko, M. Donowitz, Cholera toxin inhibits SNX27-retromer-mediated delivery of cargo proteins to the plasma membrane. *J. Cell Sci.* **131**, jcs218610 (2018).
84. A. N. Vagnozzi, J. G. Li, J. Chiu, R. Razmpour, R. Warfield, S. H. Ramirez, D. Praticò, VPS35 regulates tau phosphorylation and neuropathology in tauopathy. *Mol. Psychiatry* (2019).
85. S. Eleuteri, A. Albanese, VPS35-based approach: A potential innovative treatment in Parkinson's disease. *Front. Neurol.* **10**, 1272 (2019).
86. D. Ringe, G. A. Petsko, What are pharmacological chaperones and why are they interesting? *J. Biol.* **8**, 80 (2009).
87. T. A. Cardote, A. Ciulli, Cyclic and macrocyclic peptides as chemical tools to recognise protein surfaces and probe protein-protein interactions. *ChemMedChem* **11**, 787–794 (2016).
88. Z. Qian, P. G. Dougherty, D. Pei, Targeting intracellular protein-protein interactions with cell-permeable cyclic peptides. *Curr. Opin. Chem. Biol.* **38**, 80–86 (2017).
89. A. Zorzi, K. Deyle, C. Heinis, Cyclic peptide therapeutics: Past, present and future. *Curr. Opin. Chem. Biol.* **38**, 24–29 (2017).
90. A. A. Vinogradov, Y. Yin, H. Suga, Macrocyclic peptides as drug candidates: Recent progress and remaining challenges. *J. Am. Chem. Soc.* **141**, 4167–4181 (2019).
91. D. S. Nielsen, N. E. Shepherd, W. Xu, A. J. Lucke, M. J. Stoermer, D. P. Fairlie, Orally absorbed cyclic peptides. *Chem. Rev.* **117**, 8094–8128 (2017).
92. J. M. Rogers, T. Passioura, H. Suga, Nonproteinogenic deep mutational scanning of linear and cyclic peptides. *Proc. Natl. Acad. Sci. U.S.A.* **115**, 10959–10964 (2018).
93. L. J. Walport, R. Obexer, H. Suga, Strategies for transitioning macrocyclic peptides to cell-permeable drug leads. *Curr. Opin. Biotechnol.* **48**, 242–250 (2017).
94. R. D. Teasdale, D. Loci, F. Houghton, L. Karlsson, P. A. Gleeson, A large family of endosome-localized proteins related to sorting nexin 1. *Biochem. J.* **358**, 7–16 (2001).
95. B. M. Collins, C. F. Skinner, P. J. Watson, M. N. Seaman, D. J. Owen, Vps29 has a phosphoesterase fold that acts as a protein interaction scaffold for retromer assembly. *Nat. Struct. Mol. Biol.* **12**, 594–602 (2005).
96. R. Ghai, M. Tello-Lafoz, S. J. Norwood, Z. Yang, T. Clairfeuille, R. D. Teasdale, I. Mérida, B. M. Collins, Phosphoinositide binding by the SNX27 FERM domain regulates its localization at the immune synapse of activated T-cells. *J. Cell Sci.* **128**, 553–565 (2015).
97. T. Clairfeuille, C. Mas, A. S. M. Chan, Z. Yang, M. Tello-Lafoz, M. Chandra, J. Widagdo, M. C. Kerr, B. Paul, I. Mérida, R. D. Teasdale, N. J. Pavlos, V. Anggono, B. M. Collins, A molecular code for endosomal recycling of phosphorylated cargos by the SNX27-retromer complex. *Nat. Struct. Mol. Biol.* **23**, 921–932 (2016).
98. K. W. Teng, Y. Ishitsuka, P. Ren, Y. Youn, X. Deng, P. Ge, S. H. Lee, A. S. Belmont, P. R. Selvin, Labeling proteins inside living cells using external fluorophores for fluorescence microscopy. *eLife* **6**, e25460 (2017).
99. Y. Cui, J. M. Carosi, Z. Yang, N. Ariotti, M. C. Kerr, R. G. Parton, T. J. Sargeant, R. D. Teasdale, Retromer has a selective function in cargo sorting via endosome transport carriers. *J. Cell Biol.* **218**, 615–631 (2019).
100. W. Kabsch, XDS. *Acta Crystallogr. D Biol. Crystallogr.* **66**, 125–132 (2010).
101. P. R. Evans, G. N. Murshudov, How good are my data and what is the resolution? *Acta Crystallogr. D Biol. Crystallogr.* **69**, 1204–1214 (2013).
102. A. J. McCoy, R. W. Grosse-Kunstleve, P. D. Adams, M. D. Winn, L. C. Storoni, R. J. Read, Phaser crystallographic software. *J. Appl. Crystallogr.* **40**, 658–674 (2007).

103. P. D. Adams, P. V. Afonine, G. Bunkóczi, V. B. Chen, I. W. Davis, N. Echols, J. J. Headd, L. W. Hung, G. J. Kapral, R. W. Grosse-Kunstleve, A. J. McCoy, N. W. Moriarty, R. Oeffner, R. J. Read, D. C. Richardson, J. S. Richardson, T. C. Terwilliger, P. H. Zwart, PHENIX: A comprehensive Python-based system for macromolecular structure solution. *Acta Crystallogr. D Biol. Crystallogr.* **66**, 213–221 (2010).
104. V. B. Chen, W. B. Arendall III, J. J. Headd, D. A. Keedy, R. M. Immormino, G. J. Kapral, L. W. Murray, J. S. Richardson, D. C. Richardson, MolProbity: All-atom structure validation for macromolecular crystallography. *Acta Crystallogr. D Biol. Crystallogr.* **66**, 12–21 (2010).
105. C. Notredame, D. G. Higgins, J. Heringa, T-Coffee: A novel method for fast and accurate multiple sequence alignment. *J. Mol. Biol.* **302**, 205–217 (2000).
106. H. Ashkenazy, S. Abadi, E. Martz, O. Chay, I. Mayrose, T. Pupko, N. Ben-Tal, ConSurf 2016: An improved methodology to estimate and visualize evolutionary conservation in macromolecules. *Nucleic Acids Res.* **44**, W344–W350 (2016).
107. L. Holm, P. Rosenstrom, Dali server: Conservation mapping in 3D. *Nucleic Acids Res.* **38**, W545–W549 (2010).
108. B. Carragher, N. Kisseberth, D. Kriegman, R. A. Milligan, C. S. Potter, J. Pulokas, A. Reilein, Leginon: An automated system for acquisition of images from vitreous ice specimens. *J. Struct. Biol.* **132**, 33–45 (2000).
109. S. Q. Zheng, E. Palovcak, J. P. Armache, K. A. Verba, Y. Cheng, D. A. Agard, MotionCor2: Anisotropic correction of beam-induced motion for improved cryo-electron microscopy. *Nat. Methods* **14**, 331–332 (2017).
110. K. Zhang, Gctf: Real-time CTF determination and correction. *J. Struct. Biol.* **193**, 1–12 (2016).
111. J. Zivanov, T. Nakane, B. O. Forsberg, D. Kimanius, W. J. H. Hagen, E. Lindahl, S. H. W. Scheres, New tools for automated high-resolution cryo-EM structure determination in RELION-3. *eLife* **7**, e42166 (2018).
112. E. F. Pettersen, T. D. Goddard, C. C. Huang, G. S. Couch, D. M. Greenblatt, E. C. Meng, T. E. Ferrin, UCSF Chimera—A visualization system for exploratory research and analysis. *J. Comput. Chem.* **25**, 1605–1612 (2004).
113. K. E. Chen, V. A. Tillu, M. Chandra, B. M. Collins, Molecular basis for membrane recruitment by the PX and C2 domains of class II phosphoinositide 3-kinase-C2α. *Structure* **26**, 1612–1625.e4 (2018).

Acknowledgments: We acknowledge the use of the Australian Microscopy and Microanalysis Research Facility at the Centre for Microscopy and Microanalysis at The University of Queensland. We also acknowledge use of the University of Queensland Remote Operation Crystallization and X-ray (UQ ROCX) Facility and the assistance of G. King and K. Byriel. X-ray data were collected on the MX1 and MX2 microfocus beamline at the Australian Synchrotron. Cryo-EM data were collected at the Vanderbilt Center for Structural Biology Cryo-Electron Microscopy Facility. We thank S. Collier and M. Chambers for data collection support. **Funding:** This work is supported by funds from the Australian Research Council (ARC) (DP160101743, DP180103244, and CE140100011), National Health and Medical Research Council (NHMRC) (APP1156493 and APP1156732), and Bright Focus Foundation (A2018627S). B.M.C. is supported by an NHMRC Senior Research Fellowship (APP1136021), D.P.F. is supported by an NHMRC Senior Principal Research Fellowship (1117017), R.G.P. is supported by an NHMRC Senior Principal Research Fellowship (APP1058565) and by the Australian Research Council Centre of Excellence in Convergent Bio-Nano Science and Technology, and D.A.S. is supported by an NHMRC Career Development Fellowship (APP1140851). This work was also supported by the Japan Agency for Medical Research and Development (AMED), Platform Project for Supporting Drug Discovery and Life Science Research (JP20am0101090), and the Japan Society for the Promotion of Science (JSPS), Specially Promoted Research (JP20H05618) to H.S. Some of this work was performed at the National Center for Cryo-EM Access and Training (NCCAT) and the Simons Electron Microscopy Center located at the New York Structural Biology Center, supported by the NIH Common Fund Transformative High Resolution Cryo-Electron Microscopy program (U24 GM129539), and by grants from the Simons Foundation (SF349247) and NY State Assembly. A.K.K., B.X., and L.P.J. are supported by NIH R35GM119525. L.P.J. is a Pew Scholar in the Biomedical Sciences, supported by the Pew Charitable Trusts. **Author contributions:** K.-E.C., T.P., and B.M.C. conceived the study. K.-E.C. and Q.G. performed protein preparation, biochemical characterization, assays, protein crystallography, and structural analysis. T.A.H. and T.P. performed peptide synthesis and some biochemical characterization supervised by D.P.F., and H.S.. Y.C., Z.Y., and S.F. performed cell-based experiments supervised by R.G.P., R.D.T., and B.M.C. Mass spectrometry work was performed by J.S. supervised by D.A.S. A.K.K. and L.P.J. performed cryo-EM work with input from K.-E.C. and B.M.C. R.J.H., M.D.H., J.S., S.J.N., B.X., and R.C.R. did experimental work and/or provided essential reagents. K.-E.C., R.D.T., T.P., and B.M.C. supervised the research. Manuscript and figures were prepared by K.-E.C. and B.M.C., with input from N.L., R.G., L.P.J., and T.P. **Competing interests:** The authors declare that they have no competing interests. **Data and materials availability:** Crystal structural data have been deposited at the PDB under the accession number 6XS5 (hVPS29–RT-D1), 6XS7 (hVPS29–RT-D2), 6XS8 (ctVPS29–RT-D3), 6XS9 (hVPS29–RT-L1), and 6XSA (hVPS29–RT-L2). Cryo-EM data have been deposited at the Electron Microscopy Data Bank (EMDB) under accession numbers EMDB-24964 and EMDB-24963 for the apo and RT-L4–bound Retromer complexes, respectively. All data needed to evaluate the conclusions in the paper are present in the paper and/or the Supplementary Materials.

Submitted 4 January 2021
Accepted 14 October 2021
Published 1 December 2021
10.1126/sciadv.abg4007